Title

How Does Water Dissociation Work in Bipolar Membranes?

Journal

Journal of the American Chemical Society, 148(23)

ISSN

0002-7863

Authors

Wu, Yifan

Stovall, T Nathan

Xi, Dawei

et al.

Publication Date

2026-06-02

DOI

10.1021/jacs.6c05146

How Does Water Dissociation Work in Bipolar Membranes?

Yifan Wu[1,2,‡], T. Nathan Stovall[1,2,‡], Dawei Xi[1,2], Shujin Hou[1,2,3], Prasad Sarma[3], Olivia T. Vulpin[3], Sayantan Sasmal[3], Adam Z. Weber[2], Justin C. Bui[1,2,4*], Shannon W. Boettcher[1,2,3*]

[1] *Department of Chemical & Biomolecular Engineering and Department of Chemistry, University of California, Berkeley, CA 94720, USA*

[2] *Energy Technologies and Systems Division, Lawrence Berkeley National Lab, Berkeley, California 94720, USA*

[3] *Department of Chemistry and Biochemistry and the Oregon Center for Electrochemistry, University of Oregon, Eugene, OR 97403, USA*

[4] *Department of Chemical and Biomolecular Engineering, New York University Tandon School of Engineering, Brooklyn, NY 11201, USA*

‡ *Denotes equal contribution*

Abstract

Bipolar membranes (BPMs) create counter-acting pH and electrostatic-potential gradients in electrochemical systems, enabling applications for pH regulation, electrocatalysis, and separations. At the polarized, interfacial junctions of a BPM, the water dissociation (WD, $2H_2O \rightleftharpoons H_3O^+ + OH^-$) reaction can be driven, but it remains poorly understood. In this Perspective, we integrate molecular insights from bulk-water autoionization and field effects with continuum descriptions of BPM electrostatics and recent WD kinetics analyses. Pristine BPM junctions highlight both the limits of field-only acceleration and the practical challenges of junction stability at extreme reverse bias. Introducing heterogeneous catalyst layers, most commonly metal oxides and graphene oxides, accelerate WD by orders of magnitude through hypothesized coupled effects: *i*) surface acid–base functionality and hydroxyl-site density mediate proton-transfer steps, and *ii*) catalyst mobile electronic/ionic charges redistribute the junction potential drop, shaping local electric fields and reactive microenvironments. Kinetic analyses suggest two regimes of heterogeneous WD mechanism, including field-driven ordering of interfacial water and a Second Wien–type dissociation barrier lowering. We conclude by defining the key unknown variables (local pH, electrostatic potential, catalyst charge state and connection between mechanisms) and outlining experimental and multiscale modeling strategies needed for predictive WD catalysis and related ion-transfer reactions.

1. Introduction

Bipolar membranes (BPMs), first reported in 1956,[1] are constructed by laminating an anion-exchange layer (AEL), containing mobile counter-anions not tethered to the polymer (usually OH^- during operation) and polymer-bound cations, with a cation-exchange layer (CEL), containing mobile counter-cations (usually H_3O^+, sometimes abbreviated as H^+ in literature) and polymer-bound anions. A key feature of BPMs is their selective ion-transport and maintenance of steady-state pH gradients, where H_3O^+ migrates through the acidic CEL and OH^- migrates through the alkaline AEL.[2] . Ion selectivity in each membrane layer is achieved by the Donnan potential established between the ion-exchange membrane and the adjacent electrolyte, which thermodynamically excludes co-ions (*i.e.*, ions with the same charge as the membrane fixed groups).

BPMs typically operate in reverse bias where current flows from AEL to CEL, with water dissociation (WD, $2H_2O \rightleftarrows H_3O^+ + OH^-$) happening between the AEL and the CEL, generating incipient OH^- (through the AEL) and H_3O^+ (through the CEL) ions that separate *via* an outward flux from the bipolar junction (**Figure 1a**). BPMs can also operate in forward bias where current flows from CEL to AEL, with water formation (WF) happening between the AEL and the CEL, generating H_2O that is formed in the bipolar junction via an inward flux of H_3O^+ (through the CEL) and OH^- (through the AEL) ions. Catalysts are introduced between the CEL and the AEL to lower the overpotential of WD and sometimes WF (**Figure 1b**).[3-9] The remarkable improvement in BPM voltage efficiencies[3,5-7,9,10] in the past decade has allowed BPMs to emerge as promising performance-competitive platforms for multiple applications, even at high currents (0.5 – 2 A cm^{-2}) not previously possible, including water electrolysis for H_2 production,[5,11-14] electrodialysis for onsite acid/base synthesis,[15-17] metal refining/recovery,[18,19] CO_2 capture and reduction,[20-27] flow batteries,[28-31] fuel cells,[32-35] and others. Applications and engineering of BPMs have been discussed in detail in other Reviews.[36-39] Here, we focus primarily on the foundational chemistry and physics relevant to WD in BPMs.

Despite these well demonstrated applications, the key reaction happening in the BPM under reverse bias, WD, is not well understood. WD is a foundational and broadly important chemical reaction. For example, the activities of carbonic anhydrase,[40-42] alkaline hydrogen evolution reaction,[43-45] electrochemical reduction of CO_2,[46] and water-gas shift reaction[47,48] are reported to be strongly related to the WD kinetics. *Indeed, all*

reactions where H_2O serves as a proton donor require embedded WD steps. In homogenous solution, WD proceeds via spontaneous heterolytic bond cleavage mediated by fluctuations of the hydrogen-bond network (**Figure 2**).[49] On heterogenous catalysts, WD is known to be accelerated,[1-12] yet the precise mechanisms are unclear and require further study of the chemistry and physics of the active interfaces.[13-15] The well-defined bipolar interface within the BPM provides a unique experimental platform to study WD kinetics, which can be difficult to isolate in other systems.[6,9,10,50,51] Investigations of WD in BPMs can advance BPM technology and catalyst development, and more broadly, provide insights into the mechanistic underpinnings of ion-generation and ion-transfer reactions at polarized interfaces, which transcend any particular application.

In this Perspective we focus on WD within the bipolar junction, discussing the known and unknown fundamental chemistry and physics of this field-driven ion-transfer phenomenon. We first discuss the autoionization of bulk H_2O as a baseline fundamental microscopic picture for understanding WD. Next, we put forth a simple continuum model of BPMs that demonstrates the underlying physics that must be considered for confined WD in BPMs. This framework is bridged to our present understanding of WD in BPMs without catalysts. We then discuss the role of heterogenous WD catalyst that we hypothesize can mediate proton-transfer events and we explore the role of interfacial electric fields. Methods for characterization of WD reactions in BPMs are summarized along with gaps in the presently available techniques. We end by highlighting unknown chemistry and physics of WD in BPMs and identifying areas for future investigation.

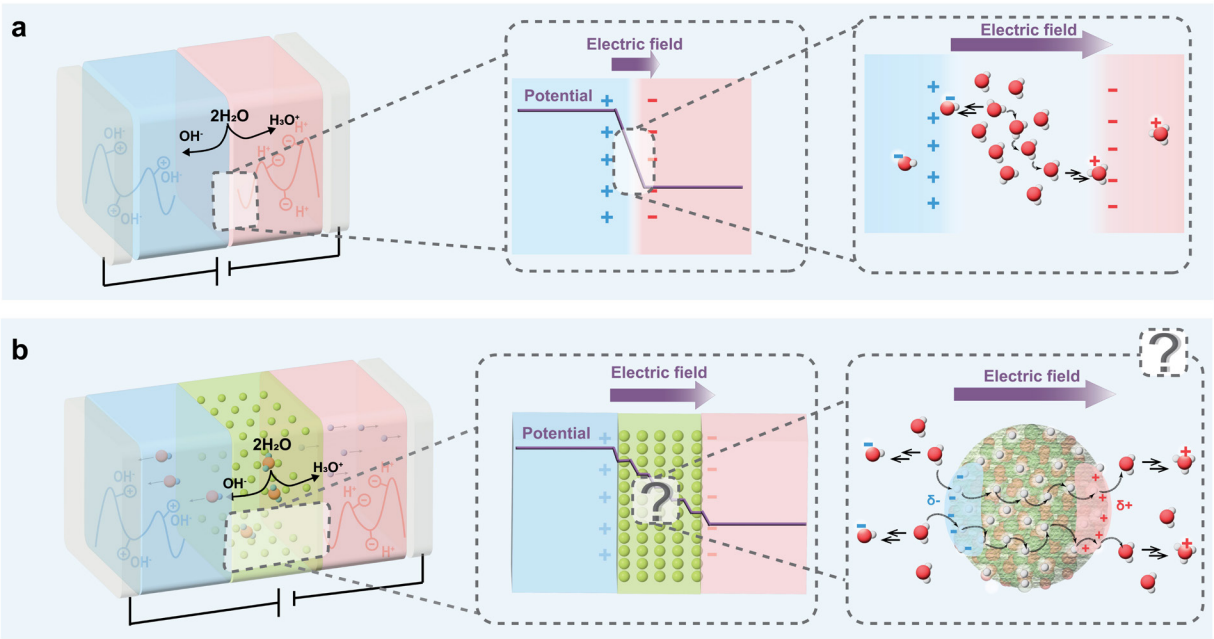

Figure 1. Conceptual macro- and microscopic pictures relevant to WD in pristine and catalyzed bipolar membranes. **(a)** WD in a pristine (catalyst-free) BPM under reverse bias. The uncompensated fixed charges create a sharp macroscopic electrostatic potential drop (middle) that facilitates WD kinetics (right). **(b)** BPM WD in the presence of a volumetric catalyst layer. The thickened junction reduces the macroscopic junction-averaged electric field, though the exact continuous potential profile across this heterogeneous layer remains a critical unknown (highlighted by the "?" in the middle panel). At the microscopic scale (right), catalyst particles may undergo electronic charge redistribution under the applied field, generating local interfacial fields that facilitate water pre-organization for proton transfer. The second "?" highlights that the detailed atomistic mechanism of surface-mediated proton transfer remains an open question explored in later sections. Blue and red regions denote the AEL and CEL, respectively. All molecular depictions are schematic and are intended only to illustrate electric fields, interfacial interactions, and representative pathways; they do not depict the exact atomistic mechanism or solvation structure.

2. Molecular physics of WD: from homogenous water to interfaces

Bulk H_2O continuously undergoes dissociation and recombination at equilibrium with the associated state favored due to the small equilibrium constant K_w. Accordingly, in water, a single WD event for a given molecule occurs every ~10 h ($k_{\mathrm{dis}} \approx 10^{-3}\ \mathrm{M\,s^{-1}}$).[52] This rate is slow relative to the timescales of solvent fluctuations (femtoseconds) and hydrogen-bond rearrangements (picoseconds).[49]

When autoionization does occur, the system rapidly traverses the reaction coordinate. Eigen and de Maeyer concluded that the rate-limiting step in autoionization is the formation of a rare intermediate microstate with a specific hydrogen-bonding network and solvation environment.[52] Subsequent molecular dynamics simulations

by Geissler and Chandler illustrated the molecular details of autoionization.[49] They show that autoionization can proceed from a large ensemble of configurational microstates, so long as the configuration generates a transient local electric field sufficiently strong to cleave an O-H bond to produce OH^- and H^+. The H^+ is transferred in a concerted fashion to a neighboring H_2O molecule forming H_3O^+. Subsequent ion separation proceeds *via* the sequential interconversion between covalent and hydrogen bonds (generically, *via* the Grotthuss mechanism[53,54]) to facilitate charge transport. Because the transient electric field persists only on femtosecond timescales, most ion-pairs rapidly recombine upon field quenching. Only when the transient electric field coincides with a disruption of the hydrogen-bonding network between the liberated ions, are the ions solvated and remain separated. When the solvated ions reach a critical contact distance along a hydrogen-bonding wire, they rapidly recombine along a near-barrierless reaction coordinate. Recent simulations further suggest that nuclear quantum effects are also important, as proton zero-point motion and delocalization increase access to proton-shared configurations and facilitate proton transfer along hydrogen-bonded networks. In this sense, autoionization is governed not only by rare solvent configurations and local electric fields, but also by the quantum mechanical nature of proton motion.[55,56]

Externally applied electric fields can also result in net H_2O ionization. Early experiments by Wien show that the conductivity of weak electrolytes increase under large electric fields (by ~10%),[57] and Onsager later rationalized these results through a theory of the field-induced enhancement of the dissociation constant.[58] In this framework, the dissociation constant shifts towards ionization as the electric field can stabilize the charge-separated state during WD and decrease the recombination probability. In the context of a reaction coordinate this can be viewed as (*nominally enthalpic*) stabilization of charge-separated transition-state.[4] This phenomenon is referred to as the Second Wien Effect (**Figure 2b**). The physical picture of the Second Wien Effect, traditionally, has been that large electric fields can weaken O-H bonds lowering the energy barrier (lower E_a in the Arrhenius equation $k = A * \exp\left(-\frac{E_a}{RT}\right)$) for WD.

Recently, Litman and Michaelides used *ab initio* molecular dynamics to provide an alternative view. They show that the WD reaction is entropically hindered in the absence of a field but becomes entropy-driven under strong electric fields.[59] At high fields, the reactant state is ordered with water molecules aligned with the field

and exhibit both stronger, and more, hydrogen bonds. Consequently, when the electric field is sufficiently strong, WD can be entropically favorable ($\Delta S > 0$). The entropy-driven physical picture illustrates that the stronger electric field organize the water molecules, making WD faster (higher A in the Arrhenius equation $k = A * \exp\left(-\frac{E_a}{RT}\right)$). Thus, even in the context of bulk autoionization, the detailed mechanistic underpinnings of WD are still unclear.

At heterogeneous interfaces, the molecular coordinates relevant to WD are complicated by broken solvent symmetry, altered hydrogen-bond networks, and interfacial electric fields. Studies at the air|water interface, and water under nanoconfinement, show that proton solvation and acid–base behavior can differ from the bulk, including interfacial stabilization of excess protons and increased interfacial Brønsted acidity.[60-62] Deep-neural-network molecular dynamic simulations at TiO_2|electrolyte interfaces suggest that electric fields primarily bias the interfacial ensemble toward dissociation-competent configurations, rather than strongly altering the barrier of an individual event.[63] On Pt, nuclear quantum effects have been shown to enhance surface-mediated WD primarily through zero-point-energy lowering, thereby stabilizing proton-delocalized configurations along interfacial hydrogen-bonded wires.[64] These results support the view that interfacial WD is governed by a collective free-energy landscape shaped by solvation structure, electrostatics, and the quantum nature of protons.

Non-ideal solvent interactions can also impact H_2O reactivity when significant ion-coordination changes the solvent properties. For example, Xu *et. al.*, show that electrolyte cations can tune the rate of the Volmer step ($H_2O + e^- \rightarrow H^* + OH^-$) in the hydrogen evolution reaction. Cations can change the acidity of hydrated water and therefore the Volmer step, but also impacts the rate of OH^- exchange through the solvation environment.[65] In concentrated electrolytes, Guha et al. showed that increasing KOH concentration increases the fraction of tetrahedrally coordinated H_2O and is accompanied by slower HER kinetics, which they interpret as a larger barrier to the Volmer step.[66] For a more comprehensive analysis of ion-effects in electrocatalysis we point the readers elsewhere.[67-69]

These studies show that WD is governed by a free-energy landscape that depends, at a minimum, on electrostatics, solvation structure, and proton dynamics. Whether field-enhanced WD is best viewed through charge-separated-state stabilization, reactant pre-organization, or suppression of recombination is unclear, even for simple systems. These knowledge gaps are amplified in BPMs, where WD occurs within a confined and

electrostatically/chemically heterogeneous junction. The central question, then, is how these concepts translate to BPMs, and which descriptors are most relevant under operating conditions. Further, prevailing questions lie in the interplay between interfacial solvent, WD catalyst chemistry (when present), and bipolar junction electrostatics.

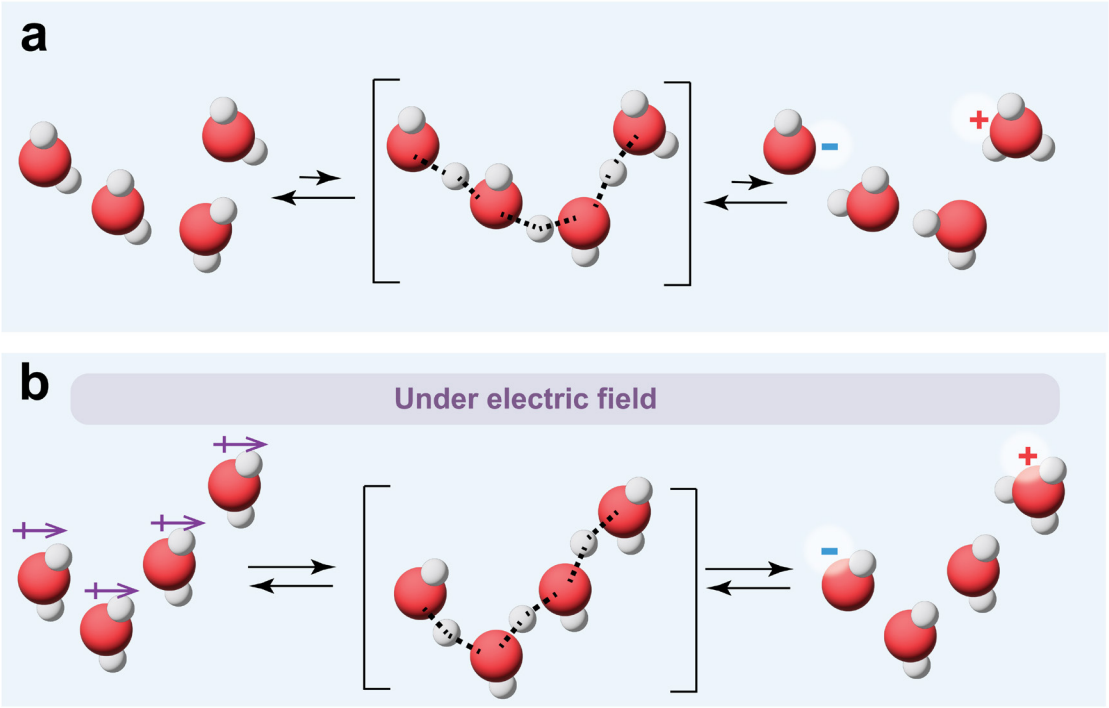

Figure 2. Molecular mechanisms of WD in bulk water. (a) Autoionization of bulk water via a Grotthuss mechanism. **(b)** Field-assisted WD in bulk water, where the applied electric field pre-organizes dipolar water molecules (purple arrows) into, on average, more-favorable proton-transfer configurations and facilitates ion separation. This picture is related to the classical Second Wien effect.[57,58] All molecular depictions are schematics and are intended only to illustrate electric fields, interfacial interactions, and representative proton-transfer pathways; they do not depict the exact atomistic mechanism or solvation structure.

3. Electrostatics and transport in the BPM junction microenvironment

Interrogating WD within the bipolar junction requires an *a priori* description of the continuum electrostatics and transport that define the baseline environment inside the BPM. Here we present a minimal 1-D continuum model of the BPM (**Figure 3a**), with more details presented in the previous work.[9] This model does not account for the complexities of integrating a catalyst within the bipolar junction, which are discussed later.

We consider the reversible reaction $2H_2O \rightleftharpoons H_3O^+ + OH^-$ with forward and reverse rate constants k_{dis} and k_{rec} and treated as independent of electric field. At equilibrium the forward and reverse rates (R) are equal,

$$R_{dis} = R_{rec} \tag{1}$$

and are related to the rate constants and the relevant species activities (a_i, where i is the species identity) per,

$$R_{dis} = k_{dis} a_{H_2O}^2 \tag{2}$$

$$R_{rec} = k_{rec} a_{H_3O^+} a_{OH^-} \tag{3}$$

Importantly, Equations 2 and 3 preserve a thermodynamically consistent, unitless equilibrium constant (Equation 4), which in turn requires that kinetic expressions maintain their activity basis and thus account for non-idealities (*e.g.*, the full chemical potential of species). Taking a_{H_2O} as unity, which is standard assignment for a pure solvent and is reasonably assumed when H_3O^+ and OH^- activities are small, $K_w \sim 10^{-14}$.

$$K_w = \frac{k_{dis}}{k_{rec}} = \frac{a_{H_3O^+} a_{OH^-}}{a_{H_2O}^2} \approx 10^{-14} \tag{4}$$

Eigen and de Maeyer, using transient voltage measurements, measured k_{rec} to be $\sim 10^{11}$ M s^{-1} (converted to activity basis).[52] From this, k_{dis} can be calculated as shown below.

$$k_{dis} = K_w k_{rec} = 10^{-3} \text{ M s}^{-1} \tag{5}$$

Throughout, thermodynamic quantities are expressed on an activity basis. In a dilute limit, however, activities may be approximated by the ratio of the relevant intensive variable (X_i, concentration, pressure, etc...) relative to a reference state (X_i^0) if the activity coefficient (γ_i) approaches unity.

$$a_i = \gamma_i \left(\frac{X_i}{X_i^0} \right) \tag{6}$$

Now, considering away from equilibrium, the net generation rate of ionic species is the difference in forward and reverse reaction rates.

$$R_{H_3O^+} = R_{OH^-} = k_{dis} a_{H_2O}^2 - k_{rec} a_{H_3O^+} a_{OH^-} \tag{7}$$

Conservation of mass through the continuity equation demands that at steady state the divergence in species flux of species i (J_i) equals R_i

$$\nabla \cdot J_i = R_i \tag{8}$$

The flux of species i is described as the gradient of its electrochemical potential ($\bar{\mu}_i$, Equations 9 and 10).

$$\bar{\mu}_i = \mu^0 + RTln(a_i) + z_i F\phi \tag{9}$$

$$\boldsymbol{J_i} = -\frac{D_i c_i}{RT}\nabla\bar{\mu}_i \tag{10}$$

Here, $\mu^0$is the standard-state chemical potential, D is the diffusion coefficient, c is concentration, z is the charge number, F is Faraday's constant, R is the gas constant, T is temperature, ϕ is the electric potential and other terms have been defined previously. Expansion of $\nabla\bar{\mu}_i$ reveals a general, and rigorous, form of the molar flux (omitting convection).

$$\boldsymbol{J_i} = -D_i\nabla c_i - D_i c_i \nabla \ln(\gamma_i) - \frac{z_i c_i F D_i}{RT}\nabla\phi \tag{11}$$

Importantly, the activity coefficient gradient ($\nabla\ln(\gamma_i)$) imparts an additional flux term due to non-idealities. When γ_i is unity, or spatially invariant, we recover the Nernst-Planck equation presented with a concentration basis (ignoring convection, Equation 12).

$$\boldsymbol{J_i} = -D_i\nabla c_i - \frac{z_i c_i F D_i}{RT}\nabla\phi \tag{12}$$

We note the assumption of unit or spatially invariant activity coefficients is a poor assumption for transport within an ionomer phase where frictional interactions between various competing ions and solvent are common,[2,70-72] yet is a useful starting point for understanding WD at the BPM junction.

Electrostatics couple to transport via the Poisson equation, which relates the charge density to the electric potential across the junction. The terms c_+ and c_- are the concentration of positive and negative charges, respectively, including mobile ions (H_3O^+ and OH^-) and fixed charges on the polymer backbone. The terms ϵ_0 and ϵ_r are relative permittivity of vacuum and bulk water, respectively. While other ions may be present in some systems[15,18,26,29,73] (such as salt species in electrodialysis) the general transport of H^+ and OH^- remain similar in the dilute limit.

$$\nabla^2\phi = -\frac{\rho_i}{\epsilon_0\epsilon_r} = -\frac{F}{\epsilon_0\epsilon_r}(\sum c_+ - \sum c_-) \tag{13}$$

Finally, the equilibrium electrochemical potential of each species must be equal across the heterojunction (*i.e.,* the definition of equilibrium). Considering H_3O^+ species, and assuming the pH in the CEL

and AEL are 0 and 14, respectively, we calculate the built-in electric potential difference necessary to maintain the pH gradient (Equation 14).

$$\Delta\phi_{\mathrm{eq}} = \frac{RT}{F}\ln\left(\frac{a_{\mathrm{H_3O^+}}^{\mathrm{CEL}}}{a_{\mathrm{H_3O^+}}^{\mathrm{AEL}}}\right) = \frac{\ln(10)\,RT}{F}\Delta pH \approx 0.83\,V\ (T = 298\ \mathrm{K}) \tag{14}$$

We define $\Delta\phi_{eq} = \phi^{\mathrm{AEL}} - \phi^{\mathrm{CEL}}$ and, following the subsequent algebra, the difference in pH is enforced as $\Delta pH = pH^{\mathrm{AEL}} - pH^{\mathrm{CEL}}$. An equivalent equilibrium can be written for OH^-.

Together, these relations define a minimal description of the catalyst-free bipolar junction, which in part acts as an ionic analogue to semiconductor *p-n* junctions,[74] with OH^- in AEL corresponding to electrons in *n*-type semiconductor, and H_3O^+ in CEL corresponding to holes in *p*-type semiconductor. When the CEL touches the AEL, the H_3O^+ (near the interface of the CEL) and OH^- (near the interface of the AEL) recombine and form charge-neutral water between the two membranes. The residual uncompensated fixed positive charges in the CEL and the residual uncompensated fixed negative charges in the AEL create a space-charge region that establishes a sharp electrostatic potential gradient across the interface over a length scale of a few nm, as opposed to the 100-1000 nm in typical semiconductor *p-n* junctions (**Figure 1a, 3a**). This process happens until the electrostatic potential gradients prevent further diffusion of H_3O^+ and OH^-, which occurs when the electrostatic potential gradient balances the chemical potential gradient, as described with Equation 11, with the electrochemical potentials of each ion equilibrating across the interface. The model outputs the spatial distribution of species electrochemical potential, concentration, electric potential and electric field across the bipolar junction, as seen in **Figure 3a**.

When the transmembrane electric potential increases, driven by the applied external field, the BPM is reverse-biased, H_3O^+ and OH^- are driven out of the heterojunction by gradients in their electrochemical potential and WD proceeds in the bipolar junction, forming new H_3O^+ and OH^-. The generation and outward-flux of H_3O^+ and OH^- reaches steady-state under constant current/voltage conditions across the BPM. The opposite is true in forward-bias, where the model predicts local enrichment in H_3O^+ and OH^- concentrations and the water formation reaction proceeds (**Figure 3a**). This is consistent with experimental results which implement a NiO_x voltametric pH probe into the BPM junction.[75]

The large electric field ($\vec{E} = -\nabla\phi$) that exists with the BPM junction has been hypothesized to lower free-energy barriers for WD in BPMs and thus impacts rates.[3,4,6,8-10,36,51] The electric-field magnitude and profile across the heterojunction are thus important. The charge carrier densities of common ionomer materials are 10^{21} cm^{-3}, corresponding to an ion exchange capacity of ~ 1 mequiv g^{-1}. Assuming an abrupt bipolar junction without a catalyst layer, this would result in a space-charge region on the order of nanometers, and therefore an electric field of ~10^8 V m^{-1}. However, polymer mobility, interfacial intermixing, and fixed-charge condensation all may result in significant deviations from those anticipated *via* the simple static 1-D model. Additional complexities arise upon inclusion of a solid nanoparticle WD catalyst layer, relative to the catalyst-free case (**Figure 1a, 1b)**. For WD in BPMs, some mechanisms are proposed and verified, as discussed in the following sections, while the actual spatial distribution of pH and the electrostatic potential profile within the BPM remain key unknowns. Non-ideal ionomer physics like ion pairing/condensation, non-unity activity coefficients, finite-size effects, and frictional coupling between ions and polymer probably significantly perturb these profiles, but the relevant parameters under bias are poorly constrained. Finally, the morphological heterogeneity implies that pH and potential involve broad distributions over interconnected water domains and tortuous ionomer–catalyst interfaces in three dimensions.

Despite the complex physics within operating BPM junctions, the typical experimentally accessible observables are limited to macroscopic quantities, namely current and trans-membrane potential difference. Accordingly, BPM WD kinetics are typically studied in either H-cell or membrane-electrode-assembly (MEA) testbeds. H-cells are experimentally simple because reference electrodes in the acid and base compartments can serve as a proxy for membrane electric potential, and therefore directly track the potential difference across the BPM as a function of current (**Figure 3b**). The bulk electrolyte reservoirs, however, can introduce complications from non-unity WD faradaic efficiency due to counter-ion crossover, and freestanding membranes are more prone to mechanical failure.[3] By contrast, MEA potential-sensing platforms (**Figure 3c, 3d**), with pure water feed, better isolate the voltage dropped across the BPM while eliminating parasitic co-ion transport and minimizing mechanical artifacts.[10] In the MEA geometry, the reference electrodes are affixed directly to AEL and CEL strips extending outside cell hardware. The WD overpotential, η_{wd}, is defined as the transmembrane electric-potential difference under current relative to the open-circuit transmembrane electric-potential

difference ($\eta_{wd} = \Delta\phi(i) - \Delta\phi(i=0)$). MEA potential-sensing measurements therefore provide a rigorous basis for defining WD overpotential and constructing quantitative rate/driving-force relationships (e.g. polarization curves, **Figure 3e**). Complementarily, electrochemical impedance spectroscopy (EIS) can separate the WD charge-transfer resistance from Ohmic contributions and other electrode reactions (**Figure 3f**). For detailed discussions on EIS data interpretation and equivalent-circuit modeling in BPMs, we direct readers to the previous work.[9]

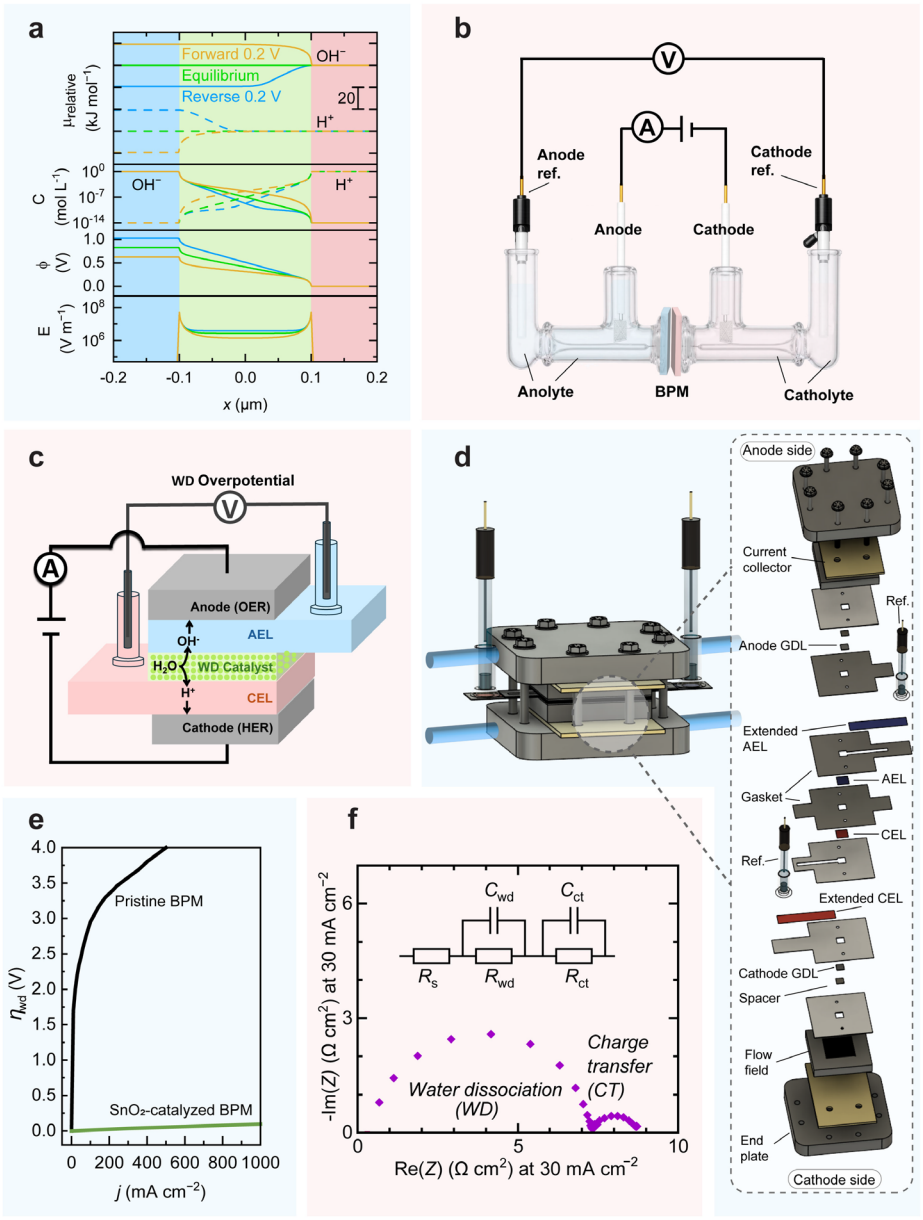

Figure 3. Experimental platforms and physical modeling used to interrogate water dissociation kinetics in BPMs. (a) A minimum physical model of the BPM junction region (representing a water-filled gap) obtained from COMSOL continuum simulations, illustrating the spatial distributions of electrochemical potential, ion concentration, electrostatic potential, and electric field across the junction region. Data are adapted from ref[9]. Available under a CC-BY 4.0 license. Copyright 2022 Springer Nature. **(b)** H-cell configuration for BPM studies in a simplified geometry. The transmembrane electric potential is measured via reference electrodes (typically equipped with Luggin capillaries to minimize uncompensated Ohmic drop), while current is applied through the anode and cathode. **(c)** Schematic of the membrane-sensing membrane-electrode-assembly (MEA) platform, in which reference electrodes are integrated on the CEL and AEL sides to isolate the voltage associated with the bipolar junction. **(d)** 3D rendered model and exploded view of the corresponding membrane-sensing cell hardware. Pure water is fed into, and flows out from, both flow fields; water transports from the flow fields into the BPM layer. **(e)** Representative WD polarization curves comparing a pristine BPM and a high-performance SnO_2-catalyzed BPM (a recent benchmark for WD activity); lower η_{wd} at a given current density indicates faster WD kinetics. Data are adapted with permission from ref[5]. Copyright 2024 Springer Nature. Additional data are adapted from ref[9]. Available under a CC-BY 4.0 license. Copyright 2022 Springer Nature. **(f)** Representative electrochemical impedance response used to extract the WD resistance, R_{wd}, from Ohmic and electrode contributions. Data are adapted from ref[9]. Available under a CC-BY 4.0 license. Copyright 2022 Springer Nature.

4. Field-driven WD in catalyst-free BPM junctions

The electric field in a pristine bipolar junction (without introducing catalysts between the AEL and the CEL) is on the order of 10^8 V m^{-1}. This large field magnitude is why the Second Wien effect (nominally enthalpic barrier reduction, discussed in Section 2) is invoked to describe field-enhanced WD. Through the Second Wien effect, electric fields can electrostatically stabilize the (fully and partially) charge-separated states that exist at the reactant and/or transition-state of WD, thereby accelerating the reaction.[4,76,77] Others, however, have argued that electric fields in bipolar junctions are insufficient to drive appreciable WD current densities. For instance, Mafé suggests that field-driven WD proceeds *via* the preferential ordering of interfacial water under an electric field, which increases the likelihood of solvent fluctuations resulting in proton transfer (i.e., an entropy effect). Therefore, experimental investigations into the relationship between enthalpic/entropic barriers for WD in BPMs are needed to mechanistically understand field-enhanced WD.

Chen[10] and Rodellar[50] each independently investigated the mechanism of rate enhancement *via* temperature-dependent WD kinetic measurements in a catalyst-free BPM.[10,50] The enthalpic and entropic barriers to WD were investigated with an Arrhenius analysis. By fitting the Arrhenius equation ($i = A * \exp\left(-\frac{E_a}{RT}\right)$), temperature-dependent measurements allow extraction of the apparent Arrhenius prefactor, A, and the apparent activation barrier, E_a, as a function of WD overpotential, η_{wd}. Through the Eyring equation, A can

be linked to the transition-state entropy barrier, $\Delta S^{\ddagger}$, and E_a to the enthalpic barrier, $\Delta H^{\ddagger}$. For uncatalyzed BPMs, Chen found that with increasing η_{wd} the E_{a} parameter was reduced (with decreased A), indicating Second-Wien-type behavior.[10] However, Rodellar et al. found the opposite, with E_{a} and A increasing with η_{wd}, indicating entropy-driven WD.[50] Thus, despite recent efforts, the underlying mechanism of WD in pristine BPMs remains uncertain, likely due to experimental complexities.

Chen, demonstrated that pristine BPM junctions exhibit unstable operation, with the polarization performance of the BPM decaying over time, likely due to degradation at the AEL|CEL interface during high overpotential operation,[10] perhaps due to field-induced interface mixing of the ionomers. This uncontrolled degradation may be the source of inconsistent results in the community. To measure reproducible and physically accurate kinetic parameters, a stable pristine AEL|CEL interface must be fabricated. Some results demonstrate that fabricating three-dimensional or roughened BPM junctions can increase performance.[78,79] Perhaps such performance increases can stabilize the BPM sufficiently to abstract kinetic parameters. Bipolar membranes composed of AEL and CEL with high chemical incompatibility might decrease interface-mixing-induced degradation.[80]

5. Coupled chemistry and electrostatics in heterogeneous WD catalysis

Oener *et al*., and others,[3,5,6,8-10,28,51,81] have demonstrated that incorporation of oxide catalysts, into the bipolar junction can increase WD rates by orders of magnitude. The rate-enhancement of WD is attributed to catalytic surface-mediated WD. In this section, we discuss the molecular-scale features of WD independent of the macroscopic junction environment. We then explore how bulk electrostatics and ion distributions across the junction are coupled to the WD catalyst chemistry, demonstrating that chemical and electrostatics effects cannot be treated independently.

Developing material design strategies for WD catalysts is challenging, however, because the activity is governed simultaneously by the catalyst surface chemistry (*e.g.*, acid-base chemistry, active-site density, etc…), and by how the materials interacts with, and subsequently controls, the electrostatic profile across the bipolar junction.[5,9,10] The chemical and electrostatic effects on WD catalysis are intrinsically coupled. For example, the

oxide acid-base properties simultaneously impact the facility of H^+ exchange, but also ionic charge build up can control the electrostatic field distribution through the heterojunction.[3,4,51]

To date, state-of-the-art WD catalyst materials are metal oxides and graphene oxides. Oxide materials typically host M-O(H)$_x$ (x = 0-2) and M-O(H)$_y$-M (y = 0-1) H^+ adsorption sites. WD is likely facilitated by a series of sequential elementary H^+ adsorption and desorption steps.[6,10,51] **Figure 1b** (right) shows a WD mechanism in which interfacial H_2O donates a H^+ to the catalyst-surface, is transported across the catalyst particle between surface-oxygen groups and finally donated to another H_2O molecule affording H_3O^+. By fabricating AEL|catalyst|AEL and the analogous CEL|catalyst|CEL architecture, Chen *et al.* find that both H^+ and OH^- transport across metal oxide catalyst layers imparted only small overpotential penalties.[9] These observations suggest the predominant overpotential penalty goes towards heterolytic water O-H bond cleavage mediated *via* the catalyst surface and separation of the incipient H^+ and OH^- ions.

The facility of H^+ adsorption/desorption during WD is rooted in the acid-base character of catalysts under a defined electrostatic field. In molecular systems, acidity is defined via a site K_a (or pK_a). For oxide surfaces, H^+ adsorption isotherms are highly non-ideal isotherms (*e.g.,* not of the Henderson Hasselbalch form) due to surface heterogeneity, lateral interactions, and charging in the diffuse layer. Thus, a single K_a is inappropriate to describe the surface acid-base properties due to significant coupling between sites. The pH of zero charge (PZC) is a more appropriate descriptor and is the pH at which the net-surface ionic charge is zero (**Figure 4a**). Acidic surfaces have a low PZC, and basic surfaces have a higher PZC. In BPMs the acid/base chemistry is further complicated by electric potential distributions across WD catalysts and their surrounding electrolytes, which can change surface acidity.

Oener *et al.* reported systematic experiments where catalyst identity was controlled on each side of the AEL|CEL junction and found that WD rates were generally enhanced when the PZC of the catalyst matched its local environment (basic surface catalysts having high PZC near the relatively alkaline AEL, and vice-versa).[6] They hypothesized that the enhancement is due to a distribution of protonation states that could accept (nominally M-O^- and M-OH) and donate (M-OH and M-OH_2^+) H^+. In that view, WD was optimized when H^+ donating and accepting functionalities co-exist under the given local conditions and thus WD catalysts work the

best if they are near the PZC. The performance trends with respect to PZC, however, had substantial scatter; and the need for further analysis was noted by the authors.

Analyzing the same datasets, Bui *et al*. used continuum modeling with Second-Wien kinetics to explore the bilayer catalyst approach invoking a chemistry-controlled electrostatics argument.[4] Here, the PZC of the WD catalyst, relative to its local environment, controls heterojunction electrostatics. For example, consider a single acidic catalyst layer integrated into the BPM. Here, there will be a larger electric field at the catalyst|AEL interface relative to the catalyst|CEL interface. If the reaction is driven electrostatically, the reaction rate will localize at the catalyst|AEL interface. The opposite is true for an alkaline catalyst. In the bilayer catalysts case Oener *et al*. reported, the reaction could localize between the two catalyst layers, and although the electric field magnitude is smaller, the reaction rate may be enhanced due to decreased bulk H^+/OH^- recombination. While the mechanistic details remain uncertain, the recognition of the interplay between catalyst chemistry and electrostatics appears a key insight.

Further evidence for the importance of transmembrane electrostatics is the U-shaped relation between BPM performance and catalyst mass loading (**Figure 4b**), which contrasts with most catalytic systems where increased active sites increase rates.[9,10,51] We hypothesize the reason for the U-shaped dependence is two-fold: *i*) at low catalyst loading, the WD becomes active-site-limited; and *ii*) at high loadings, the increased junction thickness reduces the electric field magnitude which is important for WD. Importantly, Chen *et al.* demonstrated Ohmic and transport losses are insufficient to explain high-loading limits.[9] Consistent with the electrostatic picture, more-conductive catalysts, which can screen and localize the electric field to edges of the particles or bipolar junction *via* mobile electronic charges (**Figure 4c**), have larger loading optima.[5,9] This localization of the electric field by mobile electronic charges is analogous to the behavior of mobile electrolyte ions in a solution, which redistribute in response to an applied field and confine the potential drop to interfacial regions. Likewise, inclusion of conductive (non-catalytic) carbon particles into a very thick TiO_2 (semi-insulating) catalyst layer results in performance recovery.[9,10] Stovall *et al*., show that highly ionic (acidic) graphene oxide catalyst layers have performance almost independent of loading and with the electric field and WD activity focused at the catalyst|AEL interface, consistent with Bui *et al.'s* continuum picture.

The local chemistry and electrostatics of WD catalysts are intertwined, complicating efforts to identify the origins and mechanism of WD catalytic activity. To address this, Sasmal *et al.* took a materials-screening approach to study structure-property relationship in WD catalysts.[5] Two material descriptors strongly correlated with high WD performance: *i*) the electronic conductivity of the catalyst material, and *ii*) the surface hydroxyl coverage (Γ_{OH}, the number of surface OH sites per unit area) (**Figure 4d**). The former is consistent with the previous electrostatic picture, where materials with mobile electronic charges can screen the electric field across the heterojunction and thereby are better at WD. The latter suggests it is not only the *number* of M-OH active sites, but rather the *density* of sites that determine activity. Sasmal et al.,[5] consistent with Chen,[10] proposed that densely packed hydroxyl groups form hydrogen-bonded networks that facilitate lateral H^+ translocation across the oxide surface through Grotthuss-type hopping. They argue surface H^+ mobility aids in separation of the incipient H^+ and OH^- ions. An alternative interpretation is that larger Γ_{OH} corresponds to greater surface ionic charge density and serves as an alternative modality of electrostatic screening. Regardless of the specific mechanism, Sasmal et al. used these design principles to develop a record-breaking SnO_2 WD catalyst that sustained current densities of 1.0 A cm^{-2} at ~100 mV of overpotential (**Figure 3e**).[5] The SnO_2 was synthesized via the low-temperature hydrolysis of $SnCl_4$, which gave reasonable electronic conductivity and high Γ_{OH}.

Although catalyst conductivity, surface-OH density and acid–base properties correlate with WD performance, the causal chain is ambiguous because both chemistry, electrostatics and WD activity change together. The surface protonation states modify charge densities and thus the local field, while electronic/ionic polarization can localize (or smear) the potential drop across the catalyst layer. Consequently, for most catalysts, we do not yet confidently know if the "active interface" is the catalyst|AEL, catalyst|CEL, catalyst|water nanogap, or an internal catalyst|catalyst boundary in bilayer systems, nor do we know how that location shifts with loading, hydration, and current density. Equally unresolved is how microscopic potential gradients across catalyst particles relate to catalytic turnover. Do polarized particles amplify local fields to realize entropically or enthalpically driven WD? Answering these questions requires direct measurement with self-consistent modeling of catalyst-layer potential maps together with local pH gradients and site protonation under bias. Viewing WD along only a single material axis is certainly insufficient to build a complete model of the material design

properties for WD catalysts. The following section will build, and expand, upon these concepts working towards understanding how electrostatic driving forces can drive ion-transfer or reactions.

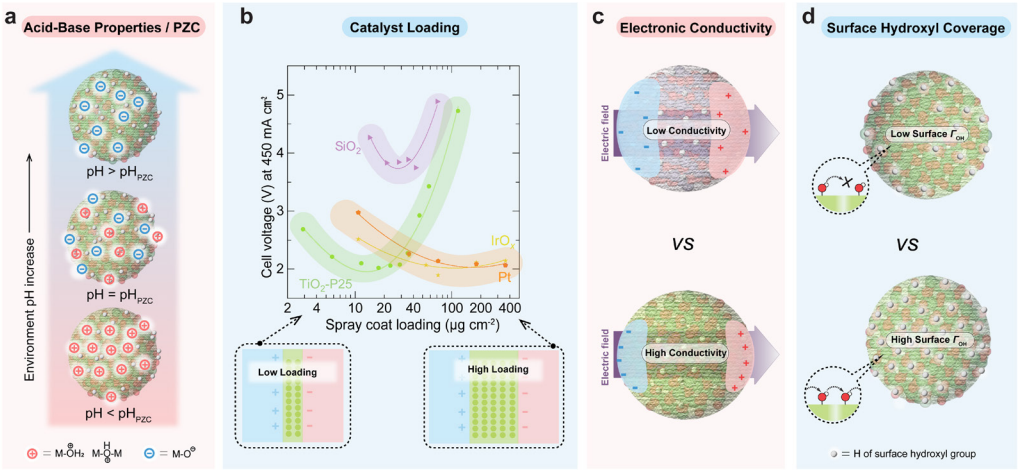

Figure 4. Catalyst descriptors for catalyzed BPM WD. **(a)** Acid-base properties / point of zero charge (PZC) as a descriptor of catalyst protonation state and charge regulation relative to the local pH environment in the junction. **(b)** Catalyst loading (or catalyst-layer thickness) as a descriptor of the tradeoff between active-site availability and junction thickening. This tradeoff gives rise to the illustrated U-shaped performance trends, which vary significantly with material conductivity, highlighting typical patterns for insulators (SiO_2), semiconductors (TiO_2-P25), and metallic conductors (IrO_x and Pt). Data are adapted from ref[9]. Available under a CC-BY 4.0 license. Copyright 2022 Springer Nature. **(c)** Catalyst conductivity as a descriptor of how the catalyst redistributes the junction potential drop and local interfacial electric fields. **(d)** Surface hydroxyl coverage as a descriptor of the density and connectivity of proton-transfer-active surface sites. It shows that adjacent -OH communication is prohibited when coverage is low, but allowed at high surface OH coverage.

6. Enthalpy or entropy driven WD in catalyzed BPMs

There is no broadly established kinetic formalism for field-driven ion-transfer reactions. Arrhenius formalisms can be used to deconvolute enthalpic and entropic contributions to reaction rates without prescribed mechanistic underpinnings. The Arrhenius equation, $j = A * \exp\left(-\frac{E_a}{RT}\right)$, relates the reaction rate to an apparent prefactor, A, which denotes the reaction attempt frequency, and E_a, the apparent activation barrier (R and T are the gas constant, and temperature, respectively). Several groups have explored mechanism-agnostic kinetic studies to explore WD as a model field-driven ion-transfer reaction.[10,50,51]

Chen *et al.*[10] and Rodellar *et. al.*[50] performed such analyses using metal oxide catalyst layers. They reported that metal-oxide-catalyzed WD polarization curves in BPMs are approximately linear as a function of η_{wd}.[10,50] This behavior is distinct from classical electrochemical kinetics, which typically show an exponential

dependence of rate on driving force. For metal oxides, despite several material differences, two common kinetic signatures can be observed: *i*) the apparent activation energy, E_a, was nominally constant with driving force (**Figure 5a**), and *ii*) the attempt frequency scales linearly with η_{wd} (**Figure 5b**). Chen *et al.* found for TiO_2 that E_a was ~25-30 kJ mol^{-1}.[10] Record-breaking SnO_2 catalysts have an E_a of ~15 kJ mol^{-1}.[5] Bulk recombination of H_3O^+ and OH^- have a barrier of 8-15 kJ mol^{-1},[82,83] which perhaps entails a lower-limit activation barrier for WD. Rodellar reported compensation between A and E_a (often coined entropy-enthalpy compensation) across catalyst materials.[50] That is, at a given η_{wd}, plotting $\log(A)$ vs E_a for different catalyst materials show a linear relationship. The molecular-scale mechanisms underpinning this result remain unclear.

These results have largely been interpreted within the context of the Eyring-Polanyi equation.[84,85] Here, E_a is proportional to the enthalpic transition-state barrier, $\Delta H^{\ddagger}$, and A is proportional to the exponential of the entropic transition-state barrier, $exp(\Delta S^{\ddagger})$. Thus, the above results indicate the electric field across the heterojunction is insufficient to appreciably reduce $\Delta H^{\ddagger}$. Although still a hypothesis, the prevailing physical interpretation is that increased driving force, and thus electric field, order interfacial H_2O at the catalyst surface.[10,50,51] This entails a reduction in the reactant entropy (S^{reactant}), and thereby $\Delta S^{\ddagger}$ ($= S^{\ddagger} - S^{\text{reactant}}$) becomes more positive and A grows in magnitude. More generally, the increase in A is suggestive of an increased likelihood of the system being in a microstate that is competent for WD. Entropically driven WD, as mentioned above, was posited via Litman et. al. in bulk H_2O simulations.[59] Chen *et al.* put forth a physical picture in which dielectric TiO_2 particles polarize in response to the macroscopic electric field across the junction.[10] Correspondingly, this field-screening can localize electric fields to the near-surface regime of the WD catalyst, resulting in entropy-driven enhanced WD under reverse bias. Although still a hypothesis, this appears consistent with the electronic conductivity trends found by Sasmal *et al*.[5] This physical picture is also consistent with that of Mafé ,[86] who proposed interfacial electric fields in BPMs are insufficient to reduce the H^+-transfer barrier, and that the origin of field-enhancement is due to cooperative ordering of interfacial water molecules.

Kinetic-isotope experiments provide further evidence for entropically driven WD in BPM. During D_2O dissociation experiments in BPMs, the η_{wd} necessary to sustain a given current is 2-4 times larger than that of H_2O.[10] The rate decrease is due to the Arrhenius prefactor A for D_2O being smaller (Figure 5b, hollow dots), supporting a picture in which the applied field increases the population of reactant configurations competent for

WD. Interestingly, Chen finds that E_a is slightly reduced for D_2O dissociation relative to H_2O (Figure 5a, hollow dots). For bulk water dissociation, the H/D E_a isotope effect is ~0.9. The slight decrease in E_a for D_2O could be due to the surface mediation of WD and the relative binding energy of H^+ vs D^+ with the surface. Nonetheless, these results are consistent with entropically driven WD, and suggest isotope effects are related to the probability of the collective environment reaching WD-competent configurational microstates.

The previous results were demonstrated primarily on systems that used catalyst layers 100 nm or more in thickness where the electrostatic potential gradient is presumably smeared across the heterojunction. A key remaining question was how the response would change in the limit of ultra-thin bipolar junctions. Yamamoto reported molecularly thin nanosheet catalyst layers[87] and found noticeably curved polarization response. They hypothesized that a sufficiently narrow bipolar junction can possibly recover Second-Wien type behavior.

Graphene oxide catalysts can behave similarly during WD in BPMs. Stovall *et al.* found that even for thick (100s on nm) graphene oxide catalyst layers, A is constant within error and that E_a is reduced linearly with overpotential.[51] The data was fit to a linear-free-energy relationship, $E_a(\eta_{\mathrm{wd}}) = E_a^0 - \alpha F \eta_{\mathrm{wd}}$, where E_a^0 is the zero-bias barrier, and α represents the fraction of the applied driving force that lowers the barrier.[51] For graphene oxide, $\alpha \approx$ 0.5-0.7 depending on the fitting approach, whereas for metal oxides $\alpha \approx 0$, consistent with previous publications. The work also showed the graphene oxide used contained significant acidic protons. Solving the modified Poisson-Nernst-Planck equation with explicit treatment of the graphene oxide protonation-state shows a sharp field localization to the AEL|graphene-oxide interface.[3] At this interface the large field appears to drive Second-Wien kinetics that speed WD.

Voltage-driven WD in BPMs thus cannot be described via a single universal kinetic response. When the electrostatic potential across the BPM is distributed, WD occurs in a low-field limit where the field-induced rate-enhancement stems from interfacial H_2O ordering. In the limit of very narrow bipolar junctions, imparted via either ultrathin catalyst layers or significant ionic field-screening, the high-field rate-enhancement appears and is assigned to Second-Wien type kinetics. Ultimately, it is the coupling of the catalyst chemistry and electrostatic environment that controls the kinetic response.

Arrhenius parameters extracted from temperature-dependent measurements provide valuable information, but the molecular-scale physical picture underpinning these *apparent* macroscopic parameters remain unclear.

For example, the direct assignment of A to the entropic transition-state barrier cannot be universally justified. In multi-step catalytic reactions, the apparent value of A may include contributions from changes in the pre-rate-determining-step equilibria, active site populations/identities, transport processes, ion separation/recombination dynamics, or other phenomena, such that A may contain both entropic and enthalpic contributions. Similarly, any temperature-dependence to the aforementioned processes would appear in the apparent E_a term. The role of overpotential/current-dependence of local pH/potential distributions and mass transport on the Arrhenius parameters are yet to be established. For example, measured increase in A with overpotential could reflect reduced interfacial reactant entropy, but it could also arise from bias-dependent growth of the active interfacial area or mass transport. It is unknown whether field-induced water ordering is sufficient to explain the magnitude of rate enhancement on leading catalysts, or whether additional energetic stabilization (including specific chemical bonding or nominal proton-coupled electron transfer, PCET) must be invoked. Further, the BPM junction is non-ideal and hosts low-activity interfacial water; it is unclear which interfacial H_2O molecules undergo dissociation and how they transport through the distinct hydrogen bonding environment. All of these factors can influence the apparent Arrhenius parameters measured.

Care also must be taken when considering the data quality and fits, which rely on fitting two parameters often from relatively small datasets spanning a small temperature window. When possible, larger temperature regimes should be interrogated and high-quality fits should be demonstrated. Slope-intercept covariance of linear Arrhenius fits can give rise to artificial entropy-enthalpy compensation behavior, thus claims regarding compensation behavior, particularly when only modest changes occur, should be made with caution, as discussed in the enzyme catalysis community. [88] Connecting the Arrhenius parameters to first-principles predictions will require simulations that connect physics from atomic chemistry to nano-scale molecular dynamics in the solvent to micron/nano-scale transport phenomena, while also accounting for the non-ideal thermodynamics of confined aqueous ions.

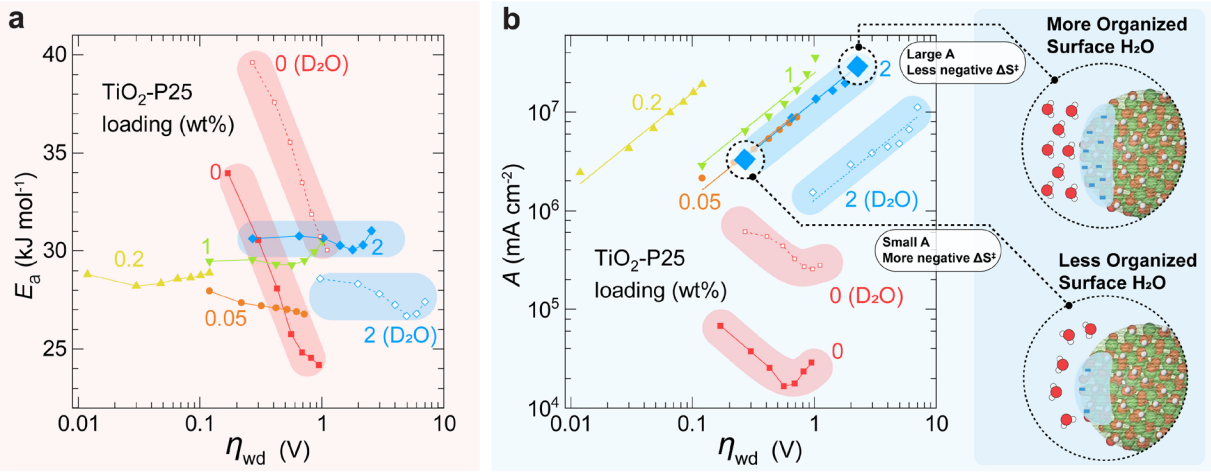

Figure 5. Apparent kinetic parameters for BPM WD. (a) Apparent activation energy, E_a, versus WD overpotential, η_{wd}, for pristine (0 wt%, red) and TiO_2-P25 catalyzed BPMs at various loadings, including selected D_2O data. **(b)** Apparent Arrhenius pre-exponential factor, A, versus η_{wd} for pristine (0 wt%, red) and TiO_2-P25 catalyzed BPMs at various loadings, including selected D_2O data. The schematic at right illustrates the interpretation on 2% TiO_2-P25 BPM WD data, showing an increasing driving force, η_{wd}, enhances interfacial water organization. This ordering lowers the reactant entropy (S_r), making the activation entropy ($\Delta S^{\ddagger} = S^{\ddagger} - S_r$) less negative and thereby increasing A. In both panels, the numerical labels and color coding correspond to the catalyst loading (wt% of the precursor ink used for spin-coating). Data for D_2O (*hollow symbols)* are presented alongside H_2O (*solid symbols*) to illustrate kinetic isotope effects. Shaded regions are guides to the eye. Data are adapted with permission from ref[10]. Copyright 2023 Elsevier.

7. Remaining unknowns and outlook

The challenges that face deeper understanding of BPMs are shared across many related ionomer-based electrochemical systems and electrified ion-transfer processes. In our discussion above, the key variables within operating BPMs, including the local electrostatic potential, electric field, and the activities of both H^+ and OH^-, which are likely out of equilibrium are inferred rather than directly measured. Research to understand the various WD dissociation mechanisms on catalyzed surfaces should be coupled to accurate measurements of at least some of these parameters during operation.

(i) ***Operando* mapping of pH and electrostatic potential distributions**. The key unknown is the bias-dependent pH and electric potential distribution within the bipolar junction. These two fields jointly define the local electrochemical potentials that govern proton transfer and ion separation. *In-situ* mapping of such nanoscale buried fields is a "holy grail" in electrochemistry more broadly.

In BPMs, the active bipolar junction is buried which makes *operando* characterization difficult. Many BPMs cannot operate in a free-standing geometry, and those that can generally require interpenetrating

geometries, supports, or adhesives that complicate the interface. Compressed MEAs are a useful platform for studying BPM complexities by minimizing mechanical side effects. Previous studies have overcome the challenge of measuring buried interfaces in the context of H_2O and CO_2 electrolysis by engineering windows into the MEA.[89] Care should be taken to develop analytical techniques with the requisite spatial resolution because junctions are typically of sub-micron thickness and morphologically heterogeneous.

With an appropriate BPM MEA platform, a suite of *operando* spectroscopic techniques can be leveraged. Local electric fields can be found by quantifying the vibrational Stark Effect.[90-92] Stark-active species on the catalyst surface, for example carbonyl or cyano groups, undergo an electric-field-induced vibrational frequency shift which can then be related to the electric field.[91,92] Raman scattering,[93-95] infrared spectroscopy,[96,97] laser-scanning confocal microscopy,[98,99] and fluorescence spectroscopy[100,101] have been used to measure pH gradients with dyes. Measuring pH gradients can inform on the local catalytic microenvironment, and thus the relative pH versus surface PZC of the catalyst. Alternatively, pH or electric-field-sensitive redox polymers or oxides can be integrated into the bipolar junction and their voltammetry can be tracked *operando via* a separate sensing circuit.[102-105] Hou *et al.* demonstrated that NiO_x and ferrocene redox probes can together track pH and electric potential within a BPM with temporal and spatial resolution.[75] Integration of this platform with mechanistic experimental campaigns will be valuable.

As opposed to interrogating the buried interface directly, a different approach would be to create 2-D BPM model structures using nanofabrication techniques. In this geometry, the BPM would effectively sit on a chip, giving a direct cross-sectional view of the device. Atomic force microscopy, and all the associated multifunctional variants, could be used for direct imaging of the BPM junction during operation. Kelvin probe microscopy could directly report on the electrostatic gradients across the device. Upon realization of this geometry, a suite of spectro/microscopic techniques could be used to directly interrogate the BPM with a cross-section geometry.

Laser-induced temperature-jump experiments might also be explored to probe the interfacial structure/entropy of H_2O within the bipolar junction.[106-108] The laser can induce a transient “temperature jump” subsequently disordering the water (increasing entropy). The water structure then relaxes back to its steady-state structure, the rate of which can be measured due to its relationship to current through the catalyst layer (as double

layer charging) or potential. These measurements could be further coupled to temperature-dependent Arrhenius experiments, relating interfacial water entropy to A directly.

Furthermore, systematic *operando* studies varying electrolyte concentration and ion identity will be crucial to determine how specific ion effects, charge–countercharge condensation, and altered interfacial water structure modulate local fields and WD kinetics in operating junctions.[109-111]

(ii) **Understanding the potential drop between WD catalysts and the junction electrolyte.** A key unknown is the relative potential of catalyst particles (and their internal polarization) versus the adjacent electrolyte, and how this potential distribution depends on catalyst conductivity, ionic charge regulation, and loading. Multi-physics simulations for model catalysts with a defined nanostructure would be useful. Porous electrode theories, taking account of solution and solid phase potentials, should be used to build models that couple reaction microkinetics to transport and electric field distribution. WD in BPMs is a coupled reaction–transport problem where the observed overpotential reflects not only the elementary O–H cleavage step but also ion separation and flux through (typically tortuous) pathways. Models need experimental values for site densities, protonation energetics (including distributions of pK_a values, or proton absorption isotherms), local permittivity, electronic/ionic conductivities within the catalyst layer and nonideal solution behavior.

(iii) **Model catalysts with orthogonalized control for different WD mechanisms.** To interrogate specific material property/function relationships, designed model WD catalysts can be explored. WD catalysts with precise crystalline surfaces and bulk structure would provide a platform for the aforementioned *operando* investigations, as well as *ex-situ* material characterization. Systematic material design of defects/dopants to control electronic properties, exposed facets to control surface hydroxyl/proton-transfer chemistry, surface area, and morphology might help deconvolute the set of material design features that yield systematic control over the reaction rate. Surface acid-base sites can be modulated *via* precision surface-chemical functionalization without changing the bulk catalyst electronic structure. These model catalysts could be designed to study entangled mechanisms. For example, could a series of systematically varied catalyst chemistries be used to step from entropy-driven WD to a Second-Wien-effect controlled mechanism and show how the two apparent operative modalities of field enhancements exist on a continuum?

It is interesting to consider other related mechanisms for WD. For example, when using very electronically conductive catalysts, the observed voltage-dependent WD in BPMs could be caused by mechanisms involving not only proton transfer, but also formal electron transfer.[112-114] It is possible that WD may occur *via* two proton coupled electron transfer (PCET) reactions on opposite sides of WD catalysts. For example, near the AEL|catalyst side, one H_2O transfers a proton to the catalyst's surface *via* PCET to generate charge-neutral hydrogen (electron-proton pair) adsorbed on the catalyst and a free hydroxide anion, which transports across the AEL. The hydrogen could subsequently diffuse toward the catalyst|CEL interface, where opposite interfacial bias exists to oxidize the hydrogen, releasing a proton released in water and transporting across the CEL, and a free electron that migrates towards the AEL to complete the circuit. Rate-limitation of either PCET step, or the hydrogen atom flux, could alternatively explain the exponential or linear *j-E* curves. This mechanism requires electron flow and this is only possible for conductive WD catalysts. More generally, however, the degree to which electrons compensate emerging H^+ charge during catalysis likely exists on a continuum that is catalyst dependent. Likewise, it remains unclear how WD in BPMs differs from WD at electrodes, for example, Oener demonstrated the WD catalysts can accelerate alkaline HER catalysis.[6]

(iv) **From first principles to next-generation membrane materials.** Arrhenius/Eyring analyses show that voltage can tune, overall, *effective* activation entropies and/or enthalpies, but the microscopic origin remains unclear because water structure is rarely observed directly. *Ab initio* molecular dynamics and enhanced-sampling techniques under applied field could compute free-energy profiles and separate contributions from water ordering, transition-state stabilization, and recombination suppression. The challenge is to perform these calculations under realistic boundary conditions (surface charge regulation, finite ion activities, constant-potential constraints and other non-idealities) to compute accurate enthalpy/entropy changes that can be compared quantitatively to experiment.

In addition to catalysts, advancements in the bulk ionomeric materials that comprise the BPM can improve BPM performance.[8,115,116] Because state-of-the-art WD catalysts (e.g., SnO_2) now operate at overpotentials < 100 mV at 1 A cm^{-2}, the WD overpotential is no longer the primary bottleneck. Future improvements in energy efficiency and current efficiency can target the limits of the AEL and the CEL themselves by minimizing Ohmic resistance and mitigating co-ion crossover.[5] By tuning the pK_a of the interfacial ionomers, engineering the

junction morphology via electrospinning or crosslinking, and modulating water uptake properties, WD rates can be tuned. Fundamentally understanding the electrostatics of 3D interpenetrating junctions and relations between charged polymer and electric-field driven WD would be interesting and should facilitate the development of membranes for CO_2 capture/reduction, electrodialysis, and other separation applications with ultra-fast WD and WF rates.

8. Conclusion

Present Understanding. BPMs provide a quantitative platform to study WD as a field-driven ion-transfer reaction in a confined ionic heterojunction. Minimal continuum electrostatics predicts nanometer-scale space-charge regions and junction fields on the order of 10^8 V m^{-1}, but pristine junctions still require large overpotentials and can exhibit instability under sustained reverse bias. Introducing heterogeneous WD catalyst layers, particularly metal oxides, lowers the WD overpotential and enables high-rate operation at > 1 A cm^{-2}. Across catalysts and architectures, performance trends indicate that WD is governed by a coupled set of variables that include catalyst acid–base chemistry (often proxied by PZC), hydroxyl-site density and connectivity, catalyst-layer thickness/loading, and the ability of electronic or ionic polarization within the catalyst layer to redistribute and localize the junction electric potential drop. Temperature-dependent kinetics analysis implies that voltage-driven rate enhancement can arise either primarily through bias-dependent increases in the apparent attempt frequency (consistent with field-induced pre-organization of interfacial water) or, in the limit of strongly localized potential drops, through Second Wien Effect barrier lowering.

Future Opportunities. It remains unclear how the macroscopic observables, including j–V response, junction AC impedance, and temperature dependent rates, map onto the microscopic variables that control WD. These include the spatial distributions of H^+/OH^- activities and electrostatic potential within the catalyst layer and adjacent ionomers, the relative potential of catalyst particles versus junction electrolyte (including charge storage, polarization, and possible band bending), and the identity/location of the dominant reactive interface as a function of hydration, loading, and current density. Likewise, the mechanistic decomposition of apparent activation enthalpy and entropy into contributions from water ordering, transition-state charge separation, surface proton/hydroxide transport, and ion separation/recombination remains incomplete. Addressing these

gaps will require operando mapping of buried junction fields and pH, model catalysts with orthogonal control of PZC/hydroxyl density/conductivity, and multiscale simulations that couple first-principles proton-transfer energetics to continuum transport all of which must capture the non-idealities present in the complex heterojunction. Such work is not only key to enabling predictive WD catalyst design, but more broadly for understanding and controlling ion-transfer chemistry in polarized microenvironments across electrochemical systems and technologies.

Author Information

Corresponding Authors

Shannon W. Boettcher, boettcher@berkeley.edu

Justin C. Bui, justinbui@nyu.edu

Notes

The authors declare no competing financial interest.

Acknowledgment

This Perspective was written with support from the US Department of Energy, Center for Ion Management in Electrochemical Systems, Award DE-SC0024713. Y.W. and T.N.S. contributed equally to this work. T.N.S. acknowledges support from the National Science Foundation Graduate Research Fellowship (NSF-GRFP) under Grant No. DGE 2146752. J.C.B. acknowledges funding support from the Schmidt Science Fellowship. We acknowledge Lihaokun Chen for his input on the initial outline of this Perspective. We thank Yogesh Surendranath and colleagues in the Energy Conversion group at Lawrence Berkeley Laboratory, the UC Berkeley College of Chemistry, and the Oregon Center for Electrochemistry for insightful discussions that have shaped the ideas presented in this Perspective.

References

(1) Frilette, V. J. Preparation and Characterization of Bipolar Ion Exchange Membranes. *J. Phys. Chem.* **1956**, *60* (4), 435-439. DOI: 10.1021/j150538a013.

(2) Bui, J. C.; Digdaya, I.; Xiang, C.; Bell, A. T.; Weber, A. Z. Understanding Multi-Ion Transport Mechanisms in Bipolar Membranes. *ACS Appl. Mater. Interfaces* **2020**, *12* (47), 52509-52526. DOI: 10.1021/acsami.0c12686.
(3) Lucas, É.; Bui, J.; Hwang, M.; Wang, K.; Bell, A.; Weber, A.; Ardo, S.; Atwater, H.; Xiang, C. Asymmetric Bipolar Membrane for High Current Density Electrodialysis Operation with Exceptional Stability. *ACS Energy Lett.* **2023**, *9* (11), 5596–5605. DOI: 10.1021/acsenergylett.4c01662.
(4) Bui, J. C.; Corpus, K. R. M.; Bell, A. T.; Weber, A. Z. On the Nature of Field-Enhanced Water Dissociation in Bipolar Membranes. *J. Phys. Chem. C* **2021**, *125* (45), 24974–24987. DOI: 10.1021/acs.jpcc.1c08276.
(5) Sasmal, S.; Chen, H.; Sarma, P. V.; Mitchell, J. B.; Vulpin, O. T.; Wells, K. M.; Spontak, R. J.; Boettcher, S. W. Materials Descriptors for Advanced Water Dissociation Catalysts in Bipolar Membranes. *Nat. Mater.* **2023**, *23* (10), 1421-1427. DOI: 10.1038/s41563-024-01943-8.
(6) Oener, S. Z.; Foster, M. J.; Boettcher, S. W. Accelerating Water Dissociation In Bipolar Membranes and for Electrocatalysis. *Science* **2020**, *369* (6507), 1099-1103. DOI: 10.1126/science.aaz1487.
(7) Mitchell, J. B.; Chen, L.; Langworthy, K.; Fabrizio, K.; Boettcher, S. W. Catalytic Proton–Hydroxide Recombination for Forward-Bias Bipolar Membranes. *ACS Energy Lett.* **2022**, *7* (11), 3967-3973. DOI: 10.1021/acsenergylett.2c02043.
(8) Gao, T.; Schulte, L.; Xiao, L.; Yamamoto, E.; Metlay, A. S.; Sheehan, C. J.; Marth, S.; Park, H.; Sasmal, S.; Galang, F. J.; et al. Bipolar Membranes With Controlled, Microscale 3D Junctions Enhance the Rates of Water Dissociation and Formation. *Adv. Energy Mater.* **2024**, *15* (12), 2404285. DOI: 10.1002/aenm.202404285.
(9) Chen, L.; Xu, Q.; Oener, S. Z.; Fabrizio, K.; Boettcher, S. W. Design Principles for Water Dissociation Catalysts in High-Performance Bipolar Membranes. *Nat. Commun.* **2022**, *13* (1), 3846. DOI: 10.1038/s41467-022-31429-7.
(10) Chen, L.; Xu, Q.; Boettcher, S. W. Kinetics and Mechanism of Heterogeneous Voltage-Driven Water-Dissociation Catalysis. *Joule* **2023**, *7* (8), 1867-1886. DOI: 10.1016/j.joule.2023.06.011.
(11) Han, S.; Sasmal, S.; Shen, M.; Wu, Y.; Vulpin, O. T.; Hou, S.; Kim, S.; Lee, J. Y.; Yoon, J.; Boettcher, S. W. Advancing SnO2-Based Water Dissociation Catalysis in Bipolar-Membrane Water Electrolyzers. *ACS Energy Lett.* **2025**, *10* (4), 1633-1641. DOI: 10.1021/acsenergylett.5c00309.
(12) Ge, Z.; Shehzad, M. A.; Yang, X.; Li, G.; Wang, H.; Yu, W.; Liang, X.; Ge, X.; Wu, L.; Xu, T. High-Performance Bipolar Membrane for Electrochemical Water Electrolysis. *J. Membr. Sci.* **2022**, *656*, 120660. DOI: 10.1016/j.memsci.2022.120660.
(13) Hong, E.; Yang, Z.; Zeng, H.; Gao, L.; Yang, C. Recent Development and Challenges of Bipolar Membranes for High Performance Water Electrolysis. *ACS Mater. Lett.* **2024**, *6* (5), 1623-1648. DOI: 10.1021/acsmaterialslett.3c01227.
(14) Adisasmito, S.; Khoiruddin, K.; Sutrisna, P. D.; Wenten, I. G.; Siagian, U. W. R. Bipolar Membrane Seawater Splitting for Hydrogen Production: A Review. *ACS Omega* **2024**, *9* (13), 14704-14727. DOI: 10.1021/acsomega.3c09205.
(15) Bazinet, L.; Lamarche, F.; Ippersiel, D. Bipolar-membrane electrodialysis: Applications of electrodialysis in the food industry. *Trends Food Sci. Technol.* **1998**, *9* (3), 107-113. DOI: 10.1016/S0924-2244(98)00026-0.
(16) Khoiruddin, K.; Wenten, I. G.; Siagian, U. W. R. Advancements in Bipolar Membrane Electrodialysis Techniques for Carbon Capture. *Langmuir* **2024**, *40* (18), 9362-9384. DOI: 10.1021/acs.langmuir.3c03873.
(17) Fu, R.; Wang, H.; Yan, J.; Li, R.; Jiang, C.; Wang, Y.; Xu, T. Asymmetric bipolar membrane electrodialysis for acid and base production. *AIChE J.* **2023**, *69* (3), e17957. DOI: 10.1002/aic.17957.
(18) Arana Juve, J.-M.; Christensen, F. M. S.; Wang, Y.; Wei, Z. Electrodialysis for metal removal and recovery: A review. *Chem. Eng. J.* **2022**, *435*, 134857. DOI: 10.1016/j.cej.2022.134857.
(19) Luo, Y.; Liu, Y.; Shen, J.; Van Der Bruggen, B. Application of Bipolar Membrane Electrodialysis in Environmental Protection and Resource Recovery: A Review. *Membranes* **2022**, *12* (9), 829. DOI: 10.3390/membranes12090829.

(20) Disch, J.; Ingenhoven, S.; Vierrath, S. Bipolar Membrane with Porous Anion Exchange Layer for Efficient and Long-Term Stable Electrochemical Reduction of CO_2 to CO. *Adv. Energy Mater.* **2023**, *13* (38), 2301614. DOI: 10.1002/aenm.202301614.
(21) Salvatore, D. A.; Weekes, D. M.; He, J.; Dettelbach, K. E.; Li, Y. C.; Mallouk, T. E.; Berlinguette, C. P. Electrolysis of Gaseous CO_2 to CO in a Flow Cell with a Bipolar Membrane. *ACS Energy Lett.* **2018**, *3* (1), 149-154. DOI: 10.1021/acsenergylett.7b01017.
(22) Subramanian, S.; Yang, K.; Li, M.; Sassenburg, M.; Abdinejad, M.; Irtem, E.; Middelkoop, J.; Burdyny, T. Geometric Catalyst Utilization in Zero-Gap CO_2 Electrolyzers. *ACS Energy Lett.* **2023**, *8* (1), 222-229. DOI: 10.1021/acsenergylett.2c02194.
(23) Xie, K.; Miao, R. K.; Ozden, A.; Liu, S.; Chen, Z.; Dinh, C.-T.; Huang, J. E.; Xu, Q.; Gabardo, C. M.; Lee, G.; et al. Bipolar membrane electrolyzers enable high single-pass CO_2 electroreduction to multicarbon products. *Nat. Commun.* **2022**, *13* (1), 3609. DOI: 10.1038/s41467-022-31295-3.
(24) Digdaya, I. A.; Sullivan, I.; Lin, M.; Han, L.; Cheng, W.-H.; Atwater, H. A.; Xiang, C. A Direct Coupled Electrochemical System for Capture and Conversion of CO_2 from Oceanwater. *Nat. Commun.* **2020**, *11* (1), 4412. DOI: 10.1038/s41467-020-18232-y.
(25) Sullivan, I.; Goryachev, A.; Digdaya, I. A.; Li, X.; Atwater, H. A.; Vermaas, D. A.; Xiang, C. Coupling electrochemical CO_2 conversion with CO_2 capture. *Nat. Catal.* **2021**, *4* (11), 952-958. DOI: 10.1038/s41929-021-00699-7.
(26) Bui, J. C.; Lucas, É.; Lees, E. W.; Liu, A. K.; Atwater, H. A.; Xiang, C.; Bell, A. T.; Weber, A. Z. Analysis of Bipolar Membranes for Electrochemical CO_2 Capture from Air and Oceanwater. *Energy Environ. Sci.* **2023**, *16* (11), 5076-5095. DOI: 10.1039/D3EE01606D.
(27) Xi, D.; Zhao, P.; Bansal, M.; Vulpin, O. T.; Boettcher, S. W.; Aziz, M. J. Oxygen-tolerant CO_2 capture using protected redox-driven reverse bias bipolar membrane electrodialysis. *Carbon Future* **2026**. DOI: 10.26599/cf.2026.9200066.
(28) Yan, Z.; Wycisk, R. J.; Metlay, A. S.; Xiao, L.; Yoon, Y.; Pintauro, P. N.; Mallouk, T. E. High-Voltage Aqueous Redox Flow Batteries Enabled by Catalyzed Water Dissociation and Acid–Base Neutralization in Bipolar Membranes. *ACS Cent. Sci.* **2021**, *7* (6), 1028-1035. DOI: 10.1021/acscentsci.1c00217.
(29) Al-Dhubhani, E.; Pärnamäe, R.; Post, J. W.; Saakes, M.; Tedesco, M. Performance of Five Commercial Bipolar Membranes under Forward and Reverse Bias Conditions for Acid-Base Flow Battery Applications. *J. Membr. Sci.* **2021**, *640*, 119748. DOI: 10.1016/j.memsci.2021.119748.
(30) Xia, J.; Eigenberger, G.; Strathmann, H.; Nieken, U. Flow battery based on reverse electrodialysis with bipolar membranes: Single cell experiments. *J. Membr. Sci.* **2018**, *565*, 157-168. DOI: 10.1016/j.memsci.2018.07.073.
(31) Xi, D.; Alfaraidi, A. M.; Gao, J.; Cochard, T.; Faria, L. C. I.; Yang, Z.; George, T. Y.; Wang, T.; Gordon, R. G.; Liu, R. Y.; Aziz, M. J. Mild pH-decoupling aqueous flow battery with practical pH recovery. *Nat. Energy* **2024**, *9* (4), 479-490. DOI: 10.1038/s41560-024-01474-1.
(32) Peng, S.; Xu, X.; Lu, S.; Sui, P.-C.; Djilali, N.; Xiang, Y. A Self-Humidifying Acidic–Alkaline Bipolar Membrane Fuel Cell. *J. Power Sources* **2015**, *299*, 273-279. DOI: 10.1016/j.jpowsour.2015.08.104.
(33) Peng, X.; Kulkarni, D.; Huang, Y.; Omasta, T. J.; Ng, B.; Zheng, Y.; Wang, L.; LaManna, J. M.; Hussey, D. S.; Varcoe, J. R.; et al. Using Operando Techniques to Understand and Design High Performance and Stable Alkaline Membrane Fuel Cells. *Nat. Commun.* **2020**, *11* (1), 3561. DOI: 10.1038/s41467-020-17370-7.
(34) Li, Q.; Gong, J.; Peng, S.; Lu, S.; Sui, P.-C.; Djilali, N.; Xiang, Y. Theoretical design strategies of bipolar membrane fuel cell with enhanced self-humidification behavior. *J. Power Sources* **2016**, *307*, 358-367. DOI: 10.1016/j.jpowsour.2016.01.016.
(35) Ünlü, M.; Zhou, J.; Kohl, P. A. Hybrid Anion and Proton Exchange Membrane Fuel Cells. *J. Phys. Chem. C* **2009**, *113* (26), 11416-11423. DOI: 10.1021/jp903252u.
(36) Bui, J. C.; Lees, E. W.; Marin, D. H.; Stovall, T. N.; Chen, L.; Kusoglu, A.; Nielander, A. C.; Jaramillo, T. F.; Boettcher, S. W.; Bell, A. T.; Weber, A. Z. Multi-scale physics of bipolar membranes in electrochemical processes. *Nat. Chem. Eng.* **2024**, *1* (1), 45-60. DOI: 10.1038/s44286-023-00009-x.

(37) Pärnamäe, R.; Mareev, S.; Nikonenko, V.; Melnikov, S.; Sheldeshov, N.; Zabolotskii, V.; Hamelers, H. V. M.; Tedesco, M. Bipolar Membranes: a Review on Principles, Latest Developments, and Applications. *J. Membr. Sci.* **2021**, *617*, 118538. DOI: 10.1016/j.memsci.2020.118538.
(38) Blommaert, M. A.; Aili, D.; Fontananova, E.; Tufa, R. A.; Li, Q.; Smith, W. A.; Vermaas, D. A. Insights and Challenges for Applying Bipolar Membranes in Advanced Electrochemical Energy Systems. *ACS Energy Lett.* **2021**. DOI: 10.1021/acsenergylett.1c00618.
(39) Giesbrecht, P. K.; Freund, M. S. Recent Advances in Bipolar Membrane Design and Applications. *Chem. Mater.* **2020**. DOI: 10.1021/acs.chemmater.0c02829.
(40) Silverman, D. N.; Lindskog, S. The catalytic mechanism of carbonic anhydrase: implications of a rate-limiting protolysis of water. *Acc. Chem. Res.* **1988**, *21* (1), 30-36. DOI: 10.1021/ar00145a005.
(41) Silverman, D. N.; Tu, C. K.; Lindskog, S.; Wynns, G. C. Rate of exchange of water from the active site of human carbonic anhydrase C. *J. Am. Chem. Soc.* **1979**, *101* (22), 6734-6740. DOI: 10.1021/ja00516a040.
(42) Lindskog, S.; Coleman, J. E. The catalytic mechanism of carbonic anhydrase. *Proc. Natl. Acad. Sci. U. S. A.* **1973**, *70* (9), 2505-2508. DOI: 10.1073/pnas.70.9.2505.
(43) Peng, L.; Liao, M.; Zheng, X.; Nie, Y.; Zhang, L.; Wang, M.; Xiang, R.; Wang, J.; Li, L.; Wei, Z. Accelerated Alkaline Hydrogen Evolution on $M(OH)_x$/M-$MoPO_x$ (M = Ni, Co, Fe, Mn) Electrocatalysts by Coupling Water Dissociation and Hydrogen Ad-Desorption Steps. *Chem. Sci.* **2020**, *11* (9), 2487-2493. DOI: 10.1039/C9SC04603H.
(44) McCrum, I. T.; Koper, M. T. M. The Role of Adsorbed Hydroxide in Hydrogen Evolution Reaction Kinetics on Modified Platinum. *Nat. Energy* **2020**, *5* (11), 891-899. DOI: 10.1038/s41560-020-00710-8.
(45) Anantharaj, S.; Noda, S.; Jothi, V. R.; Yi, S.; Driess, M.; Menezes, P. W. Strategies and Perspectives to Catch the Missing Pieces in Energy-Efficient Hydrogen Evolution Reaction in Alkaline Media. *Angew. Chem., Int. Ed.* **2021**, *60* (35), 18981-19006. DOI: 10.1002/anie.202015738.
(46) Luo, M.; Wang, Z.; Li, Y. C.; Li, J.; Li, F.; Lum, Y.; Nam, D. H.; Chen, B.; Wicks, J.; Xu, A.; et al. Hydroxide promotes carbon dioxide electroreduction to ethanol on copper via tuning of adsorbed hydrogen. *Nat. Commun.* **2019**, *10* (1), 5814. DOI: 10.1038/s41467-019-13833-8.
(47) Yao, S.; Zhang, X.; Zhou, W.; Gao, R.; Xu, W.; Ye, Y.; Lin, L.; Wen, X.; Liu, P.; Chen, B.; et al. Atomic-layered Au clusters on alpha-MoC as catalysts for the low-temperature water-gas shift reaction. *Science* **2017**, *357* (6349), 389-393. DOI: 10.1126/science.aah4321.
(48) Yu, J.; Qin, X.; Yang, Y.; Lv, M.; Yin, P.; Wang, L.; Ren, Z.; Song, B.; Li, Q.; Zheng, L.; et al. Highly Stable Pt/CeO(2) Catalyst with Embedding Structure toward Water-Gas Shift Reaction. *J. Am. Chem. Soc.* **2024**, *146* (1), 1071-1080. DOI: 10.1021/jacs.3c12061.
(49) Geissler, P. L.; Dellago, C.; Chandler, D.; Hutter, J.; Parrinello, M. Autoionization in Liquid Water. *Science* **2001**, *291* (5511), 2121-2124. DOI: 10.1126/science.1056991.
(50) Rodellar, C. G.; Gisbert-Gonzalez, J. M.; Sarabia, F.; Roldan Cuenya, B.; Oener, S. Z. Ion solvation kinetics in bipolar membranes and at electrolyte–metal interfaces. *Nat. Energy* **2024**. DOI: 10.1038/s41560-024-01484-z.
(51) Stovall, T. N.; Bui, J. C.; Wu, Y.; Hou, S.; Boettcher, S. W.; Weber, A. Z. Electric-field enhanced water-dissociation catalysis on oxide surfaces. *EES Catalysis* **2026**. DOI: 10.1039/d5ey00364d.
(52) Eigen, M.; Maeyer, L. D. Untersuchungen über die Kinetik der Neutralisation. I. *I. Z. Elektrochem.* **1955**. DOI: 10.1002/bbpc.19550591020.
(53) Agmon, N.; Bakker, H. J.; Campen, R. K.; Henchman, R. H.; Pohl, P.; Roke, S.; Thämer, M.; Hassanali, A. Protons and Hydroxide Ions in Aqueous Systems. *Chem. Rev.* **2016**, *116* (13), 7642-7672. DOI: 10.1021/acs.chemrev.5b00736.
(54) Agmon, N. The Grotthuss mechanism. *Chem. Phys. Lett.* **1995**, *244* (5-6), 456-462. DOI: 10.1016/0009-2614(95)00905-j.
(55) Cassone, G. Nuclear Quantum Effects Largely Influence Molecular Dissociation and Proton Transfer in Liquid Water under an Electric Field. *J Phys Chem Lett* **2020**, *11* (21), 8983-8988. DOI: 10.1021/acs.jpclett.0c02581.

(56) Dasgupta, S.; Cassone, G.; Paesani, F. Nuclear Quantum Effects and the Grotthuss Mechanism Dictate the pH of Liquid Water. *J Phys Chem Lett* **2025**, *16* (12), 2996-3003. DOI: 10.1021/acs.jpclett.5c00168.
(57) Wien, M. Über eine Abweichung vom Ohmschen Gesetze bei Elektrolyten. *Annalen der Physik* **1927**, *388* (11), 327-361. DOI: 10.1002/andp.19273881103.
(58) Onsager, L. Deviations from Ohm's Law in Weak Electrolytes. *J. Chem. Phys.* **1934**, *2* (9), 599-615. DOI: 10.1063/1.1749541.
(59) Litman, Y.; Michaelides, A. Entropy Governs the Structure and Reactivity of Water Dissociation Under Electric Fields. *J. Am. Chem. Soc.* **2025**, *147* (49), 44885-44894. DOI: 10.1021/jacs.5c12397.
(60) Das, S.; Imoto, S.; Sun, S.; Nagata, Y.; Backus, E. H. G.; Bonn, M. Nature of Excess Hydrated Proton at the Water-Air Interface. *J. Am. Chem. Soc.* **2020**, *142* (2), 945-952. DOI: 10.1021/jacs.9b10807.
(61) Mishra, H.; Enami, S.; Nielsen, R. J.; Stewart, L. A.; Hoffmann, M. R.; Goddard, W. A., 3rd; Colussi, A. J. Bronsted basicity of the air-water interface. *Proc. Natl. Acad. Sci. U. S. A.* **2012**, *109* (46), 18679-18683. DOI: 10.1073/pnas.1209307109.
(62) de la Puente, M.; Laage, D. How the Acidity of Water Droplets and Films Is Controlled by the Air-Water Interface. *J. Am. Chem. Soc.* **2023**, *145* (46), 25186-25194. DOI: 10.1021/jacs.3c07506.
(63) Zhang, C.; Yu, Z.; Car, R.; Selloni, A. Tuning water dissociation at oxide-electrolyte interfaces with electric fields. *Proc. Natl. Acad. Sci. U. S. A.* **2025**, *122* (34), e2505929122. DOI: 10.1073/pnas.2505929122.
(64) Litman, Y.; Donadio, D.; Ceriotti, M.; Rossi, M. Decisive role of nuclear quantum effects on surface mediated water dissociation at finite temperature. *J. Chem. Phys.* **2018**, *148* (10), 102320. DOI: 10.1063/1.5002537.
(65) Xu, P.; Wang, R.; Zhang, H.; Carnevale, V.; Borguet, E.; Suntivich, J. Cation Modifies Interfacial Water Structures on Platinum during Alkaline Hydrogen Electrocatalysis. *J. Am. Chem. Soc.* **2024**, *146* (4), 2426-2434. DOI: 10.1021/jacs.3c09128.
(66) Guha, A.; Sahoo, M.; Alam, K.; Rao, D. K.; Sen, P.; Narayanan, T. N. Role of water structure in alkaline water electrolysis. *iScience* **2022**, *25* (8), 104835. DOI: 10.1016/j.isci.2022.104835.
(67) Bender, J. T.; Petersen, A. S.; Østergaard, F. C.; Wood, M. A.; Heffernan, S. M. J.; Milliron, D. J.; Rossmeisl, J.; Resasco, J. Understanding Cation Effects on the Hydrogen Evolution Reaction. *ACS Energy Lett.* **2022**, *8* (1), 657-665. DOI: 10.1021/acsenergylett.2c02500.
(68) Resasco, J. A Universal Model of Cation Effects in Electrocatalysis. *JACS Au* **2025**, *5* (11), 5253-5266. DOI: 10.1021/jacsau.5c01115.
(69) Monteiro, M. C. O.; Goyal, A.; Moerland, P.; Koper, M. T. M. Understanding Cation Trends for Hydrogen Evolution on Platinum and Gold Electrodes in Alkaline Media. *ACS Catal* **2021**, *11* (23), 14328-14335. DOI: 10.1021/acscatal.1c04268.
(70) Bui, J. C.; Lees, E. W.; Liu, A. K.; Toh, W. L.; Stovall, T. N.; Goyal, P.; Galang, F. J. U.; Surendranath, Y.; Bell, A. T.; Weber, A. Z. Ion-specific phenomena limit energy recovery in forward-biased bipolar membranes. *Nat. Chem. Eng.* **2025**, *2* (1), 63-76. DOI: 10.1038/s44286-024-00154-x.
(71) Crothers, A. R.; Darling, R. M.; Kusoglu, A.; Radke, C. J.; Weber, A. Z. Theory of Multicomponent Phenomena in Cation-Exchange Membranes: Part I. Thermodynamic Model and Validation. *J. Electrochem. Soc.* **2020**, *167* (1). DOI: 10.1149/1945-7111/ab6723.
(72) Crothers, A. R.; Darling, R. M.; Kusoglu, A.; Radke, C. J.; Weber, A. Z. Theory of Multicomponent Phenomena in Cation-Exchange Membranes: Part II. Transport Model and Validation. *J. Electrochem. Soc.* **2020**, *167* (1). DOI: 10.1149/1945-7111/ab6724.
(73) Chen, B.; Jiang, C.; Wang, Y.; Fu, R.; Liu, Z.; Xu, T. Selectrodialysis with bipolar membrane for the reclamation of concentrated brine from RO plant. *Desalination* **2018**, *442*, 8-15. DOI: 10.1016/j.desal.2018.04.031.
(74) Schulte, L.; White, W.; Renna, L. A.; Ardo, S. Turning water into a protonic diode and solar cell via doping and dye sensitization. *Joule* **2021**, *5* (9), 2380-2394. DOI: 10.1016/j.joule.2021.06.016.
(75) Hou, S.; Stovall, T. N.; Weber, A. Z.; Boettcher, S. W. Measuring pH Changes Inside a Bipolar Membrane Junction. *ACS Energy Lett.* **2026**. DOI: 10.1021/acsenergylett.5c03710.

(76) Mareev, S. A.; Evdochenko, E.; Wessling, M.; Kozaderova, O. A.; Niftaliev, S. I.; Pismenskaya, N. D.; Nikonenko, V. V. A Comprehensive Mathematical Model of Water Splitting in Bipolar Membranes: Impact of The Spatial Distribution of Fixed Charges and Catalyst at Bipolar Junction. *J. Membr. Sci.* **2020**, *603*, 118010. DOI: 10.1016/j.memsci.2020.118010.
(77) Strathmann, H.; Krol, J. J.; Rapp, H.-J.; Eigenberger, G. Limiting current density and water dissociation in bipolar membranes. *J. Membr. Sci.* **1997**, *125* (1), 123-142. DOI: 10.1016/S0376-7388(96)00185-8.
(78) Shen, C.; Wycisk, R.; Pintauro, P. N. High performance electrospun bipolar membrane with a 3D junction. *Energy Environ. Sci.* **2017**, *10* (6), 1435-1442. DOI: 10.1039/C7EE00345E.
(79) Al-Dhubhani, E.; Post, J. W.; Duisembiyev, M.; Tedesco, M.; Saakes, M. Understanding the Impact of the Three-Dimensional Junction Thickness of Electrospun Bipolar Membranes on Electrochemical Performance. *ACS Appl Polym Mater* **2023**, *5* (4), 2533-2541. DOI: 10.1021/acsapm.2c02182.
(80) Toh, W. L.; Chu, A. T.; Surendranath, Y. Separation of Polymeric Charge Enables Efficient Bipolar Membrane Operation. *ACS Energy Lett.* **2024**, *9* (4), 1423-1430. DOI: 10.1021/acsenergylett.4c00460.
(81) Yan, Z.; Zhu, L.; Li, Y. C.; Wycisk, R.; Pintauro, P. N.; Hickner, M. A.; Mallouk, T. E. The balance of electric field and interfacial catalysis in promoting water dissociation in bipolar membranes. *Energy Environ. Sci.* **2018**. DOI: 10.1039/c8ee01192c.
(82) Eigen, M.; De Maeyer, L. Self-dissociation and protonic charge transport in water and. *Proc. R. Soc. Lond. A. Math. Phys. Sci.* **1958**, *247* (1251), 505-533. DOI: 10.1098/rspa.1958.0208.
(83) Natzle, W. C.; Moore, C. B. Recombination of hydrogen ion (H^+) and hydroxide in pure liquid water. *J. Phys. Chem.* **1985**, *89* (12), 2605-2612. DOI: 10.1021/j100258a035.
(84) Eyring, H. The Activated Complex in Chemical Reactions. *J. Chem. Phys.* **1935**, *3* (2), 107-115. DOI: 10.1063/1.1749604.
(85) Laidler, K. J.; King, M. C. Development of transition-state theory. *J. Phys. Chem.* **1983**, *87* (15), 2657-2664. DOI: 10.1021/j100238a002.
(86) Mafé, S.; Ramírez, P.; Alcaraz, A. Electric field-assisted proton transfer and water dissociation at the junction of a fixed-charge bipolar membrane. *Chem. Phys. Lett.* **1998**, *294* (4-5), 406-412. DOI: 10.1016/S0009-2614(98)00877-X.
(87) Yamamoto, E.; Gao, T.; Xiao, L.; Kopera, K.; Marth, S.; Park, H.; Bae, C.; Osada, M.; Mallouk, T. E. Molecularly Thin Nanosheet Films as Water Dissociation Reaction Catalysts Enhanced by Strong Electric Fields in Bipolar Membranes. *J. Am. Chem. Soc.* **2025**, *147* (17), 14270-14279. DOI: 10.1021/jacs.4c17830.
(88) Cornish-Bowden, A. Enthalpy-entropy compensation and the isokinetic temperature in enzyme catalysis. *J. Biosci.* **2017**, *42* (4), 665-670. DOI: 10.1007/s12038-017-9719-0.
(89) Lu, X.; Zhou, C.; Delima, R. S.; Lees, E. W.; Soni, A.; Dvorak, D. J.; Ren, S.; Ji, T.; Bahi, A.; Ko, F.; Berlinguette, C. P. Visualization of CO_2 electrolysis using optical coherence tomography. *Nat. Chem.* **2024**, *16* (6), 979-987. DOI: 10.1038/s41557-024-01465-5.
(90) Chattopadhyay, A.; Boxer, S. G. Vibrational Stark Effect Spectroscopy. *J. Am. Chem. Soc.* **1995**, *117* (4), 1449-1450. DOI: 10.1021/ja00109a038.
(91) Fried, S. D.; Boxer, S. G. Measuring Electric Fields and Noncovalent Interactions Using the Vibrational Stark Effect. *Acc. Chem. Res.* **2015**, *48* (4), 998-1006. DOI: 10.1021/ar500464j.
(92) Fried, S. D.; Boxer, S. G. Electric Fields and Enzyme Catalysis. *Annu. Rev. Biochem.* **2017**, *86* (Volume 86, 2017), 387-415. DOI: 10.1146/annurev-biochem-061516-044432.
(93) Zhang, Z.; Bando, K.; Mochizuki, K.; Taguchi, A.; Fujita, K.; Kawata, S. Quantitative Evaluation of Surface-Enhanced Raman Scattering Nanoparticles for Intracellular pH Sensing at a Single Particle Level. *Anal. Chem.* **2019**, *91* (5), 3254-3262. DOI: 10.1021/acs.analchem.8b03276.
(94) Zong, S.; Wang, Z.; Yang, J.; Cui, Y. Intracellular pH Sensing Using p-Aminothiophenol Functionalized Gold Nanorods with Low Cytotoxicity. *Anal. Chem.* **2011**, *83* (11), 4178-4183. DOI: 10.1021/ac200467z.
(95) Lu, X.; Zhu, C.; Wu, Z.; Xuan, J.; Francisco, J. S.; Wang, H. In Situ Observation of the pH Gradient near the Gas Diffusion Electrode of CO_2 Reduction in Alkaline Electrolyte. *J. Am. Chem. Soc.* **2020**, *142* (36), 15438-15444. DOI: 10.1021/jacs.0c06779.

(96) Yang, K.; Kas, R.; Smith, W. A. In Situ Infrared Spectroscopy Reveals Persistent Alkalinity near Electrode Surfaces during CO_2 Electroreduction. *J. Am. Chem. Soc.* **2019**, *141* (40), 15891-15900. DOI: 10.1021/jacs.9b07000.
(97) Lorenz-Fonfria, V. A.; Saita, M.; Lazarova, T.; Schlesinger, R.; Heberle, J. pH-sensitive vibrational probe reveals a cytoplasmic protonated cluster in bacteriorhodopsin. *Proc. Natl. Acad. Sci.* **2017**, *114* (51), E10909-E10918. DOI: 10.1073/pnas.1707993114.
(98) Böhme, A.; Bui, J. C.; Fenwick, A. Q.; Bhide, R.; Feltenberger, C. N.; Welch, A. J.; King, A. J.; Bell, A. T.; Weber, A. Z.; Ardo, S.; Atwater, H. A. Direct observation of the local microenvironment in inhomogeneous CO_2 reduction gas diffusion electrodes via versatile pOH imaging. *Energy Environ. Sci.* **2023**, *16* (4), 1783-1795, 10.1039/D2EE02607D. DOI: 10.1039/D2EE02607D.
(99) Cope, S. J.; Hibberd, S.; Whetstone, J.; MacRae, R. J.; Melia, C. D. Measurement and Mapping of pH in Hydrating Pharmaceutical Pellets Using Confocal Laser Scanning Microscopy. *Pharm. Res.* **2002**, *19* (10), 1554-1563. DOI: 10.1023/A:1020425220441.
(100) Leenheer, A. J.; Atwater, H. A. Imaging Water-Splitting Electrocatalysts with pH-Sensing Confocal Fluorescence Microscopy. *J. Electrochem. Soc.* **2012**, *159* (9), H752. DOI: 10.1149/2.022209jes.
(101) Bleeker, J.; Kahn, A. P.; Baumgartner, L. M.; Grozema, F. C.; Vermaas, D. A.; Jager, W. F. Quinolinium-Based Fluorescent Probes for Dynamic pH Monitoring in Aqueous Media at High pH Using Fluorescence Lifetime Imaging. *ACS Sens.* **2023**, *8* (5), 2050-2059. DOI: 10.1021/acssensors.3c00316.
(102) Pöller, S.; Schuhmann, W. A miniaturized voltammetric pH sensor based on optimized redox polymers. *Electrochim. Acta* **2014**, *140*, 101-107. DOI: 10.1016/j.electacta.2014.03.116.
(103) Wachta, I.; Balasubramanian, K. Electroanalytical Strategies for Local pH Sensing at Solid–Liquid Interfaces and Biointerfaces. *ACS Sens.* **2024**, *9* (9), 4450-4468. DOI: 10.1021/acssensors.4c01391.
(104) Michalak, M.; Kurel, M.; Jedraszko, J.; Toczydlowska, D.; Wittstock, G.; Opallo, M.; Nogala, W. Voltammetric pH Nanosensor. *Anal. Chem.* **2015**, *87* (23), 11641-11645. DOI: 10.1021/acs.analchem.5b03482.
(105) Ghoneim, M. T.; Nguyen, A.; Dereje, N.; Huang, J.; Moore, G. C.; Murzynowski, P. J.; Dagdeviren, C. Recent Progress in Electrochemical pH-Sensing Materials and Configurations for Biomedical Applications. *Chem. Rev.* **2019**, *119* (8), 5248-5297. DOI: 10.1021/acs.chemrev.8b00655.
(106) Hawkins, A. P.; Edmeades, A. E.; Hutchison, C. D. M.; Towrie, M.; Howe, R. F.; Greetham, G. M.; Donaldson, P. M. Laser induced temperature-jump time resolved IR spectroscopy of zeolites. *Chem. Sci.* **2024**, *15* (10), 3453-3465, 10.1039/D3SC06128K. DOI: 10.1039/D3SC06128K.
(107) Ding, X.; Sarpey, T. K.; Hou, S.; Garlyyev, B.; Li, W.; Fischer, R. A.; Bandarenka, A. S. Prospects of Using the Laser-Induced Temperature Jump Techniques for Characterisation of Electrochemical Systems. *ChemElectroChem* **2022**, *9* (4), e202101175. DOI: 10.1002/celc.202101175.
(108) Lowe, L. B.; Brewer, S. H.; Krämer, S.; Fuierer, R. R.; Qian, G.; Agbasi-Porter, C. O.; Moses, S.; Franzen, S.; Feldheim, D. L. Laser-Induced Temperature Jump Electrochemistry on Gold Nanoparticle-Coated Electrodes. *J. Am. Chem. Soc.* **2003**, *125* (47), 14258-14259. DOI: 10.1021/ja036672h.
(109) Tian, Y.; Huang, B.; Song, Y.; Zhang, Y.; Guan, D.; Hong, J.; Cao, D.; Wang, E.; Xu, L.; Shao-Horn, Y.; Jiang, Y. Effect of ion-specific water structures at metal surfaces on hydrogen production. *Nat. Commun.* **2024**, *15* (1), 7834. DOI: 10.1038/s41467-024-52131-w.
(110) Kamcev, J.; Paul, D. R.; Manning, G. S.; Freeman, B. D. Ion Diffusion Coefficients in Ion Exchange Membranes: Significance of Counterion Condensation. *Macromolecules* **2018**, *51* (15), 5519-5529. DOI: 10.1021/acs.macromol.8b00645.
(111) Kitto, D.; Kamcev, J. Manning condensation in ion exchange membranes: A review on ion partitioning and diffusion models. *J. Polym. Sci.* **2022**, *60* (21), 2929-2973. DOI: doi.org/10.1002/pol.20210810.
(112) Ryu, J.; Bregante, D. T.; Howland, W. C.; Bisbey, R. P.; Kaminsky, C. J.; Surendranath, Y. Thermochemical aerobic oxidation catalysis in water can be analysed as two coupled electrochemical half-reactions. *Nat. Catal.* **2021**, *4* (9), 742-752. DOI: 10.1038/s41929-021-00666-2.

(113) Wang, H. X.; Surendranath, Y. Thermochemical heterolytic hydrogenation catalysis proceeds through polarization-driven hydride transfer. *Nat. Chem* **2026**, *18* (1), 43-50. DOI: 10.1038/s41557-025-01939-0.
(114) Xu, X.; Howland, W. C.; Martín-Yerga, D.; Cadaram, C. S.; Harraz, D. M.; West, G. D.; Unwin, P. R.; Surendranath, Y. Electrochemical imaging of thermochemical catalysis. *Nat. Catal.* **2026**. DOI: 10.1038/s41929-026-01486-y.
(115) Kao, Y.-L.; Buchauer, F.; Serhiichuk, D.; Boettcher, S. W.; Aili, D. Bipolar Membranes Via Divergent Synthesis: On the Interplay between Ion Exchange Capacity and Water Dissociation Catalysis. *ACS Appl. Mater. Interfaces* **2024**, *16* (43), 58637-58647. DOI: 10.1021/acsami.4c12213.
(116) Kao, Y.-L.; Chen, L.; Boettcher, S. W.; Aili, D. Divergent Synthesis of Bipolar Membranes Combining Strong Interfacial Adhesion and High-Rate Capability. *ACS Energy Lett.* **2024**, *9* (6), 2953-2959. DOI: 10.1021/acsenergylett.4c01178.

TOC Graphic

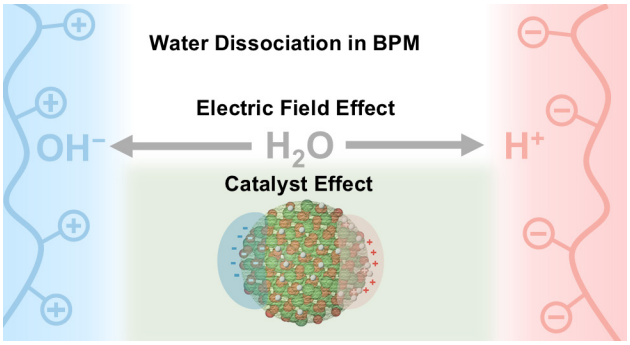
Water Dissociation in BPM
Electric Field Effect
OH⁻
H2O
H⁺
Catalyst Effect